



**HAL**  
open science

## Multiproxy reconstruction of late quaternary upper ocean temperature in the subtropical southwestern Atlantic

Joana Cruz, Ioanna Bouloubassi, Arnaud Huguet, Alice M.S. Rodrigues, Thiago Santos, Igor Venancio, Douglas Lessa, Rodrigo Sobrinho, Rodrigo Nascimento, Marcelo Bernardes

### ► To cite this version:

Joana Cruz, Ioanna Bouloubassi, Arnaud Huguet, Alice M.S. Rodrigues, Thiago Santos, et al.. Multiproxy reconstruction of late quaternary upper ocean temperature in the subtropical southwestern Atlantic. *Quaternary Science Reviews*, 2023, 307, pp.108044. 10.1016/j.quascirev.2023.108044. hal-04150017

**HAL Id: hal-04150017**

**<https://hal.science/hal-04150017>**

Submitted on 10 Oct 2023

**HAL** is a multi-disciplinary open access archive for the deposit and dissemination of scientific research documents, whether they are published or not. The documents may come from teaching and research institutions in France or abroad, or from public or private research centers.

L'archive ouverte pluridisciplinaire **HAL**, est destinée au dépôt et à la diffusion de documents scientifiques de niveau recherche, publiés ou non, émanant des établissements d'enseignement et de recherche français ou étrangers, des laboratoires publics ou privés.

1 **Multiproxy reconstruction of late Quaternary upper ocean temperature in the**  
2 **Subtropical Southwestern Atlantic**

3

4 Joana F. Cruz\*<sup>1</sup>, Ioanna Bouloubassi<sup>2</sup>, Arnaud Hugué<sup>3</sup>, Alice M. S. Rodrigues<sup>1</sup>, Thiago  
5 P. Santos<sup>1</sup>, Igor M. Venancio<sup>1</sup>, Douglas Lessa<sup>1</sup>, Rodrigo L. Sobrinho<sup>1</sup>, Rodrigo A.  
6 Nascimento<sup>1</sup>, Marcelo C. Bernardes<sup>1</sup>

7

8 <sup>1</sup>Department of Geochemistry, Federal Fluminense University, Niterói, Brazil.

9 <sup>2</sup>Laboratoire d'Océanographie et du Climat: Expérimentations et approches numériques  
10 (LOCEAN/IPSL), Sorbonne Université, Campus Pierre et Marie Curie, Paris, France.

11 <sup>3</sup>Sorbonne Université, CNRS, EPHE, PSL, UMR METIS, Paris, France.

12

13 \*Corresponding author: Joana F. Cruz (joanafcruz@gmail.com)

14

15 **ABSTRACT**

16 Paleooceanographic studies addressing the oceanographic variability in the western sector  
17 of the subtropical South Atlantic - especially those focused on the Brazil Current (BC)  
18 and on a time scale that reaches marine isotope stage (MIS) 5 - are still rare when  
19 compared with equivalent studies carried out in the Northern Hemisphere. In order to  
20 close the data gap prior to the last 75 ka, in an unprecedented approach in this region, we  
21 reconstructed the upper temperature variations in the Subtropical Southwestern Atlantic  
22 (SSWA) between late MIS 6 and the onset of MIS 4 from organic proxies, using a marine  
23 sediment core (GL-1090). Sea temperature records derived from alkenone-based  $U_{37}^K$  and  
24 isoprenoid glycerol dialkyl glycerol tetraethers (isoGDGTs)-based  $TEX_{86}^H$  proxies were  
25 compared with those previously obtained from the same core via *Globigerinoides*

26 *ruber* (*G. ruber*) Mg/Ca and planktonic foraminifera Modern Analog Technique (MAT).  
27 The temporal variations of the temperature estimates derived from the  $U_{37}^{K'}$  and  $TEX_{86}^H$   
28 indexes showed similar patterns, even though the absolute  $U_{37}^{K'}$  temperatures were  
29 systematically lower than those derived from  $TEX_{86}^H$ . Such a difference was related to the  
30 different habitat depths of alkenones and isoGDGTs source organisms of – haptophyte  
31 algae and marine *Thaumarchaeota*, respectively. The temperature estimates from  $TEX_{86}^H$   
32 match the range of Mg/Ca and MAT-derived temperatures between 0 and 10 m depth,  
33 suggesting that these proxies reflect mixed layer temperatures. In contrast, the  
34 temperature estimates derived from  $U_{37}^{K'}$  were close to the MAT values at between 0 and  
35 100 m and to those derived from  $TEX_{86}^H$  between 0 and 200 m depth, demonstrating that  
36 the  $U_{37}^{K'}$  proxy recorded temperatures from the upper thermocline. During MIS 5e, the  
37 difference in temperature estimates from  $TEX_{86}^H$  and  $U_{37}^{K'}$  was reduced due to more  
38 prominent warming, probably related to a change in the thermal structure of the photic  
39 zone. Comparison of our data with studies of intensity and salinity anomalies of the  
40 Agulhas Current indicates a connection between the intensification of the Agulhas  
41 Leakage and the heat storage in the upper thermocline in the SSWA during MIS 5e. Our  
42 data suggest that the joint use of  $TEX_{86}^H$  and  $U_{37}^{K'}$  is a promising approach to estimating  
43 paleoceanographic changes in the upper thermocline.

44

45 **KEYWORDS:** Alkenones; GDGTs; Subtropical Southwestern Atlantic; Last Interglacial

46

## 47 1. INTRODUCTION

48 Paleoclimate studies based on geochemical data contribute to climate modeling by  
49 providing a record of past natural climate oscillations beyond instrumental periods  
50 (Hansen et al., 2016; Otto-Bliesner et al., 2016). In this context, studies focusing on the

51 reconstitution of past climate variability help to understand changes that occurred in a  
52 climate similar to the present. The Marine Isotope Stage (MIS) 5e (129 - 116 thousand of  
53 years BP, hereafter – “ka”), also known as the Last Interglacial (LIG), has been widely  
54 studied in climate change investigation because it is the most recent period in which the  
55 planet was warmer than it is in the present-day and due to its similarity to the pre-  
56 industrial atmospheric greenhouse gas levels and high sea level (Turney and Jones, 2010;  
57 Capron et al., 2014; Govin et al., 2015; Otto-Bliesner et al., 2016; PAGES, 2016).

58 Paleoclimatographic studies addressing the oceanographic variability in the western  
59 sector of the subtropical South Atlantic - especially those focused on the Brazil Current  
60 (BC) and on a time scale that reaches MIS 5 - are still rare when compared with equivalent  
61 studies conducted in the Northern Hemisphere. Most of the sea surface temperature (SST)  
62 reconstructions from the BC focus on the last 75 ka (Lourenço et al., 2016; Pereira et al.,  
63 2018; Dauner et al., 2019; Luz et al., 2020) and/or the Holocene (Pivel et al., 2013;  
64 Chiessi et al., 2014; Cordeiro et al., 2014; Evangelista et al., 2014; Lessa et al., 2014;  
65 Wainer et al., 2014; Chiessi et al., 2015; Lessa et al., 2016; Luz et al., 2020). The few  
66 temperature reconstructions for the BC that include MIS 5 were obtained from single  
67 proxies, such as planktonic foraminifera transfer function and Mg/Ca ratio (Portilho-  
68 Ramos et al., 2015; Lessa et al., 2017; Santos et al., 2017a; Santos et al., 2017b).

69 Since the reconstruction of sea paleotemperatures is based on proxies derived from  
70 marine organisms, SST estimates may be affected by the ecological preferences of these  
71 organisms. The most common organic geochemical proxies used to reconstruct SSTs are  
72 (i) alkenones synthesized by haptophyta algae (Brassell et al., 1986), through the  $U_{37}^{K'}$   
73 index (Prahl and Wakeham, 1987), and (ii) isoprenoid glycerol dialkyl glycerol  
74 tetraethers (isoGDGTs) from marine *Thaumarchaeota*, through the  $TEX_{86}$  index  
75 (Schouten et al., 2002). A multiproxy SST approach can help to assess the individual

76 proxy responses and can provide more confidence in the interpretations of how climate  
77 signals are being recorded (Mann et al., 1998; Leduc et al., 2010). Moreover, applying a  
78 multiproxy reconstruction in the same sediment core will reflect conditions from the same  
79 time period without chronological uncertainties (Huguet et al., 2011; Ausín et al., 2019).

80 This study is the first reconstruction of temperature variations at the upper ocean in  
81 the Subtropical Southwestern Atlantic (SSWA) using organic proxies from late -MIS 6  
82 to the onset of MIS 4. Here, we investigated possible discrepancies in temperatures  
83 reconstructed by organic proxies, what factors may have caused such differences and we  
84 evaluated the responses of these proxies to the regional dynamics during the LIG. Sea  
85 temperatures were reconstructed from the same sediment record using the  $U_{37}^{K'}$  and  $TEX_{86}$   
86 indexes, respectively derived from alkenones and isoGDGTs. The corresponding results  
87 were compared with studies of intensity and salinity anomalies of the Agulhas Current.

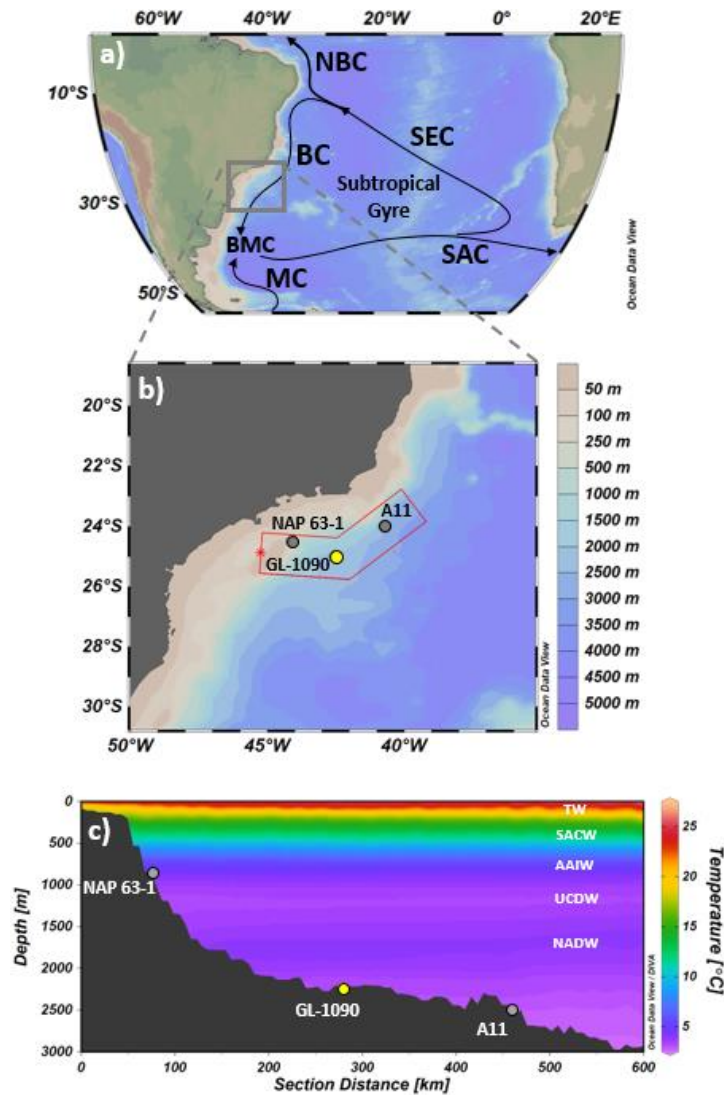
88

## 89 2. STUDY AREA

90 The Santos Basin is located on the southeastern Brazilian continental margin, limited  
91 to the north by the Campos Basin and to the south by the Pelotas Basin. The upper ocean  
92 circulation (0 - 600 m) in this region is controlled by the BC, which originates from the  
93 southern branch of the South Equatorial Current (SEC) (10 – 14 °S) (Peterson and  
94 Stramma, 1991) and flows southward along the Brazilian margin (Stramma and England,  
95 1999) (Fig. 1a). The upper layer of the BC (0 – 100 m depth) carries Tropical Water  
96 (TW) – a warm (> 20 °C), saline (> 36) and oligotrophic water mass influenced by high  
97 solar radiation, the wind field and excessive evaporation (Peterson and Stramma, 1991;  
98 Campos et al., 1995; Stramma and England, 1999; Silveira et al., 2000). The South  
99 Atlantic Central Water (SACW) corresponds to the bottom layer of the BC (100 – 600m  
100 depth; Fig. 1c) and is colder (~ 6 – 20 °C), less saline (34.6 – 36) and richer in nutrients

101 than the TW. The SACW flows in the thermocline layer and is formed in two sites: (i) in  
102 the Brazil-Malvinas Confluence (BMC) region, where the BC encounters the northward-  
103 flowing Malvinas Current (MC) (Peterson and Stramma, 1991) (Fig. 1a) and (ii) in the  
104 eastern region, via the Agulhas Leakage, bringing Indian Ocean Central Water into the  
105 South Atlantic (Richardson, 2007). The water masses that compose the deepest layers of  
106 the region are the Antarctic Intermediate Water (AAIW) (600 – 1200 m depth, northward  
107 direction), the Upper Circumpolar Deep Water (UCDW) (1200 – 1500 m depth,  
108 northward direction) and the North Atlantic Deep Water (NADW) (1500 – 2000 m depth,  
109 southward direction) (Stramma and England, 1999; Campos et al., 1995; Campos et al.,  
110 2000; Piola et al., 2000; Piola and Matano, 2001; Schmid, 2014; Silveira et al., 2000; Fig.  
111 1c).

112



113

114 Fig. 1: Oceanographic setting of the study area and location of sediment core GL-1090.

115 (a) South Atlantic surface circulation with the main currents of the South Atlantic

116 subtropical gyre: (BC) Brazil Current; (BMC) Brazil-Malvinas Confluence; (MC)

117 Malvinas (Falkland) Current; (NBC) North Brazil Current; (SAC) South Atlantic Current;

118 and (SEC) South Equatorial Current (modified from Stramma and England, 1999). (b)

119 Zoom of the study area (gray rectangle in a) with the position of core GL-1090 (this study)

120 and cores used in the discussion: downcore NAP63-1 (Dauner et al., 2019) and core-top

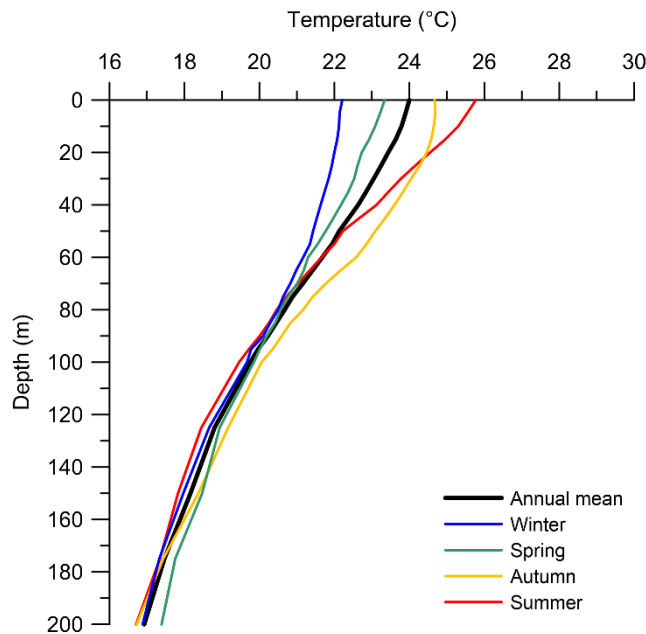
121 A11 (Ceccopieri et al., 2018). (c) Vertical section of the first 3000 m water depth of the

122 Santos Basin (highlighted red section in b) showing the cores mentioned above and the

123 water masses that compose the region: (TW) Tropical Water, (SACW) South Atlantic

124 Central Water, (AAIW) Antarctic Intermediate Water; (UCDW) Upper Circumpolar  
125 Deep Water and (NADW) North Atlantic Deep Water. This figure was partly created with  
126 the software Ocean Data View (Schlitzer, 2003). (For interpretation of the references to  
127 color in this figure legend, the reader is referred to the web version of this article.)  
128

129 Instrumental data show that the annual mean SST of the TW (0 m depth) is 24 °C, with  
130 the lowest SST (22.2 °C) during austral winter and the highest SST (25.8 °C) during  
131 austral summer (Locarnini et al., 2013). The difference in temperature between summer  
132 and winter is most pronounced in the upper 20 m of the water column (Fig. 2).  
133



134  
135 Fig. 2: Vertical profiles of the present-day temperatures in the upper 200 m of the study  
136 area provided by the World Ocean Atlas 2013 (Locarnini et al., 2013): annual mean  
137 (black), winter (blue), spring (green), autumn (yellow) and summer (red). (For  
138 interpretation of the references to color in this figure legend, the reader is referred to the  
139 web version of this article.)  
140

### 141 3. MATERIAL AND METHODS

#### 142 3.1. Sediment sampling and age model

143 The marine sediment core GL-1090 (24.92 °S, 42.51 °W, 2225 m water depth, 1914  
144 cm length) was collected by Petrobras on the continental slope of the Santos Basin (Fig.  
145 1) and stored in a refrigerated container at 4 °C. The age model, shown for the first time  
146 in Santos et al. (2017a), was based on radiocarbon dating and visual alignment of  $\delta^{18}\text{O}$   
147 from benthic foraminifera with two reference curves, MD95-4042 (Govin et al., 2014)  
148 and LR04  $\delta^{18}\text{O}$  global stack (Lisiecki and Raymo, 2005). The final age model was built  
149 using Bacon software v.2.2 (Blaauw and Christeny, 2011). Recently, Ballalai et al. (2019)  
150 and Santos et al. (2020) implemented several improvements over the original age model.  
151 Ballalai et al. (2019) chose one of the 230<sup>Th</sup> ages of the Sanbao cave as the connection  
152 point for the abrupt transition observed in the corrected ice volume  $\delta^{18}\text{O}$  at the end of  
153 Termination II. This modification, with assumes a coupling between the movements of  
154 the Intertropical Convergence Zone and the bifurcation of the South Equatorial Current  
155 in the tropical Atlantic, reduced age uncertainties from  $\pm 3.87$  to  $\pm 1.51$  ka close to the  
156 transition to the LIG. Santos et al. (2020) derived more benthic  $\delta^{18}\text{O}$  tie- points between  
157 GL-1090 and the Iberian Margin MD95-2042 (Govin et al., 2014) on the AICC2012 time  
158 scale (Bazin et al., 2013; Veres et al., 2013). The success of the new tie-points can be  
159 seen through a precise alignment between the variability on the  $\delta^{18}\text{O}$  millennial scale of  
160 *Globorotalia inflata* and NGRIP (Santos et al., 2020). Core GL-1090 spans the last 185  
161 ka. This study is focused on the age interval from 150 to 65 ka, corresponding to the depth  
162 interval from 1591 to 689 cm. Each subsample is 2 cm thick with average collection  
163 intervals of 5 cm, corresponding to an average sampling resolution of approximately 400  
164 years.

165

166 3.2. Lipid biomarker extraction and fractionation

167 Lipids were extracted from dry-frozen sediments (2 - 5 g) via three ultrasonication  
168 cycles using a solvent mixture of dichloromethane/methanol, 3:1 (v:v). The total lipid  
169 extracts were further separated into three fractions by silica gel chromatography using  
170 solvent mixtures of increasing polarity: 4 mL of hexane (elution of *n*-alkanes - not  
171 discussed in this study); 2 mL of hexane/ethyl acetate 95:5 (v:v) and then, in sequence, 2  
172 mL of hexane/ethyl acetate 90:10 (v:v) (elution of alkenones); and 5 mL of hexane/ethyl  
173 acetate 70:30 (v:v) (elution of GDGTs).

174

175 3.3. Alkenone analysis and temperature estimations

176 The fractions containing alkenones were analyzed on an Agilent 6890 Plus gas  
177 chromatograph coupled with a flame ionization detector (GC-FID), and equipped with a  
178 CPSIL-5 CB column (50 m long  $\times$  0.32 mm internal diameter  $\times$  0.25  $\mu$ m film thickness).  
179 Helium gas was used as carrier gas (2.0 mL/min). The oven was programmed with an  
180 initial temperature of 50 °C, which was then increased to 140 °C at 30 °C/min, then to  
181 280 °C at 20 °C/min, and finally to 305 °C at 0.5 °C/min. Di- and tri-unsaturated C<sub>37</sub>  
182 alkenones (C<sub>37:2</sub> and C<sub>37:3</sub>, respectively) were quantified by comparing their peak area  
183 with that of an internal standard (5 $\alpha$ -cholestane, added prior to analysis).

184 The alkenone unsaturation index  $U_{37}^{K'}$  was calculated according to Prahl and  
185 Wakeham (1987; Equation 1) and converted into temperature values using the Bayesian  
186 B-spline regression model, BAYSPLINE, for the  $U_{37}^{K'}$  paleothermometer (Tierney and  
187 Tingley, 2018), with a standard error of  $\pm 1.0$  °C.

188

189 
$$U_{37}^{K'} = \frac{C_{37:2}}{C_{37:2} + C_{37:3}} \quad (1)$$

190

191 3.4. GDGT analysis and temperature estimations

192 GDGT analyses were performed on a Shimadzu LCMS-2020 high-performance liquid  
193 chromatography-mass spectrometry (HPLC-MS) system, as recently described by  
194 Huguet et al. (2019). The semi-quantification of the GDGTs was performed by comparing  
195 the peak area of the internal standard C<sub>46</sub>GDGT with those of the compounds (cf. Huguet  
196 et al., 2013).

197 The TEX<sub>86</sub> index was calculated according to Schouten et al. (2002) (Equation 2). The  
198 numbering of the isoGDGTs refers to the publication by Kim et al. (2010).

199

$$200 \text{TEX}_{86} = \frac{\text{isoGDGT-2} + \text{isoGDGT-3} + \text{Crenarchaeol regioisomer}}{\text{isoGDGT-1} + \text{isoGDGT-2} + \text{isoGDGT-3} + \text{Crenarchaeol regioisomer}} \quad (2)$$

201

202 The annual mean sea surface temperatures (0 m) were estimated from the TEX<sub>86</sub><sup>H</sup> index  
203 (Equation 3) using the calibration by Kim et al. (2010) adapted for temperatures between  
204 15 – 30 °C, with a given uncertainty of ± 2.5 °C (Equation 4).

205

$$206 \text{TEX}_{86}^{\text{H}} = \log(\text{TEX}_{86}) \quad (3)$$

207

$$208 \text{Temp-TEX}_{86}^{\text{H}} (\text{°C}) = 68.4 (\text{TEX}_{86}^{\text{H}}) + 38.6 \quad (4)$$

209

210 The annual mean depth-integrated temperatures (0 to 200m water depth) were  
211 calculated from the global calibration by Kim et al. (2012; Equation 5), with an  
212 uncertainty of ± 2.2 °C.

213

$$214 \text{Temp-TEX}_{86}^{\text{H}}(0-200) (\text{°C}) = 54.7 (\text{TEX}_{86}^{\text{H}}) + 30.7 \quad (5)$$

215

216 The Branched and Isoprenoid Tetraether (BIT) index is suggested to represent  
217 terrestrial organic matter inputs into aquatic environments (Hopmans et al., 2004). In  
218 order to evaluate if  $\text{TEX}_{86}^{\text{H}}$  values were biased by terrigenous input at our core site, the  
219 BIT index was calculated from Hopmans et al. (2004) (Equation 6). The numbering of  
220 the branched GDGTs (brGDGTs) refer to the publication by Hopmans et al. (2004). High  
221 BIT values ( $> 0.4$ ) may lead to anomalously high  $\text{TEX}_{86}^{\text{H}}$ -derived temperatures (Weijers  
222 et al., 2006).

223

$$224 \text{ BIT index} = \frac{\text{brGDGT-I} + \text{brGDGT-II} + \text{brGDGT-III}}{\text{brGDGT-I} + \text{brGDGT-II} + \text{brGDGT-III} + \text{Crenarchaeol}} \quad (6)$$

225

## 226 4. RESULTS

### 227 4.1. Alkenone-derived temperatures ( $\text{Temp-U}_{37}^{\text{K}'}$ )

228 During the period between 150 and 65 ka, the mean  $\text{Temp-U}_{37}^{\text{K}'}$  was  $20.8 \text{ }^{\circ}\text{C} \pm 1.4$  and  
229 ranged from  $17.6 \text{ }^{\circ}\text{C}$  (ca. 146.4 ka, MIS 6) to  $26.8 \text{ }^{\circ}\text{C}$  (ca. 126.6 ka, MIS 5e) (Fig. 3a).  
230 The alkenone temperature estimates were mainly below the mean value from 150 to 140  
231 ka (MIS 6 / T II). An abrupt warming of  $6.1 \text{ }^{\circ}\text{C}$  marked the Termination II (T II), reaching  
232 a peak during MIS 5e (~127 ka), followed by a gradual cooling until mid-MIS 5d (ca. 112  
233 ka). The MIS 5e, 5c, and 5a substages generally showed warmer temperatures than MIS  
234 5d and 5b substages. The periods between ca. 82 - 79 ka and ca. 77 - 75 ka were marked  
235 by a decrease in temperature.

236

### 237 4.2. GDGT-derived temperatures ( $\text{Temp-TEX}_{86}^{\text{H}}$ , $\text{Temp-TEX}_{86}^{\text{H}}$ (0-200))

238 The mean  $\text{Temp-TEX}_{86}^{\text{H}}$  from 140 to 65 ka was  $25.4 \text{ }^{\circ}\text{C} \pm 1.4$ , ranging from  $21.1 \text{ }^{\circ}\text{C}$   
239 (ca. 68.4 ka, MIS 4) to  $28.5 \text{ }^{\circ}\text{C}$  (ca. 123.8 ka, MIS 5e) (Fig. 3a). The T II was marked by  
240 an abrupt warming of  $5.7 \text{ }^{\circ}\text{C}$ . Throughout the substages MIS 5d to MIS 5a, the

241 temperatures remained roughly stable, except for two abrupt decreases in temperature  
242 during MIS 5a. The minimum temperature was recorded at the MIS 5a / 4 (21.1 °C at  
243 69 ka). Regarding the depth-integrated temperatures, Temp-TEX<sub>86</sub><sup>H</sup> (0-200) oscillated  
244 between 16.7 °C (ca. 68.4 ka, MIS 4) and 22.7 °C (ca. 123.8 ka, MIS 5e), with an average  
245 of 20.1 °C ± 1.2 (Fig. 4).

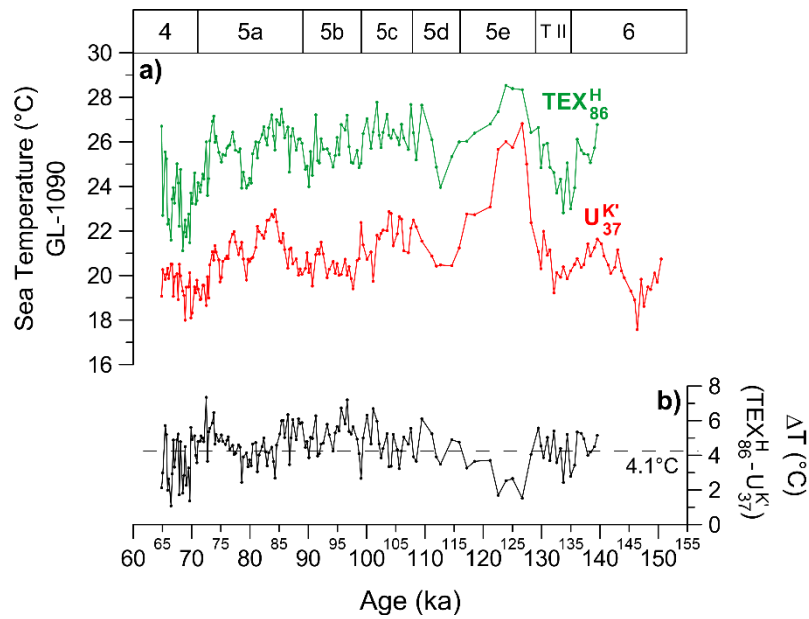
246

## 247 5. DISCUSSION

### 248 5.1. Comparison of the TEX<sub>86</sub><sup>H</sup> and U<sub>37</sub><sup>K'</sup> temperature estimates

249 In core GL-1090, similar trends were generally observed for temperatures derived  
250 from alkenones and isoprenoid GDGTs (Temp-U<sub>37</sub><sup>K'</sup> and Temp-TEX<sub>86</sub><sup>H</sup>), with a high  
251 amplitude during LIG (Fig. 3). Nevertheless, the two organic proxies provided different  
252 absolute temperature estimates. U<sub>37</sub><sup>K'</sup>-derived temperatures were systematically lower than  
253 those provided by TEX<sub>86</sub><sup>H</sup> (Fig. 3a). The peaks of Temp-U<sub>37</sub><sup>K'</sup> and Temp-TEX<sub>86</sub><sup>H</sup> were 26.8  
254 °C (126.6 ka, MIS 5e) and 28.5 °C (123.8 ka, MIS 5e), respectively, which are 2.8 °C and  
255 4.5 °C higher than the current annual mean surface temperature (0 m depth) near the GL-  
256 1090 site (Fig. 3a).

257 Turney and Jones (2010) compiled a global dataset of annual temperatures from cores  
258 spanning the LIG and deduced an increase in sea surface and terrestrial temperatures of  
259 nearly 2.0 °C above pre-industrial levels over this period. However, such warming was  
260 not uniform across the global oceans, and the SSWA was not included in the dataset.  
261 Model data performed by Otto-Bliesner et al. (2013) and sea surface temperature  
262 reconstructions published by Hoffman et al. (2017) did not indicate a significant  
263 difference in temperature during the LIG compared with the present in global tropical  
264 regions. It should be noted that these authors did not present results near our sampling  
265 site.



267

268 Fig. 3: Comparison of paleotemperatures reconstructed from isoGDGTs and alkenones:

269 a) Temp- $\text{TEX}_{86}^{\text{H}}$  (green) and Temp- $\text{U}_{37}^{\text{K}'}$  (red). The dashed line in violet marks the global  
 270 average increase during the LIG, approximately 2.0 °C relative to pre-industrial levels  
 271 (Turney and Jones, 2010). The blue dashed line marks the current annual mean sea surface  
 272 temperature in the study area (Locarnini et al., 2013); b) Temperature gradient  $\Delta T$  ( $\text{TEX}_{86}^{\text{H}}$   
 273 -  $\text{U}_{37}^{\text{K}'}$ ). The black dashed line marks the average  $\Delta T$  (4.1 °C). The marine isotopic stages  
 274 (MIS) are highlighted on the upper x-axis. (For interpretation of the references to color  
 275 in this figure legend, the reader is referred to the web version of this article.)

276

277 The peak of Temp- $\text{U}_{37}^{\text{K}'}$  from GL-1090 is consistent with the + 2.0 °C LIG surface  
 278 temperature anomaly relative to the present-day mean (Turney and Jones, 2010),  
 279 equivalent to 24 °C in the study area (Cordeiro et al., 2014; Locarnini et al., 2013). In  
 280 contrast, Temp- $\text{TEX}_{86}^{\text{H}}$  showed a very high LIG SST anomaly relative to the modern  
 281 annual mean (4.5 °C), which does not seem plausible. In order to understand the  
 282 similarities and divergences between the temperature estimates derived from  $\text{U}_{37}^{\text{K}'}$  and

283  $\text{TEX}_{86}^{\text{H}}$ , the different factors which may influence these organic proxies and their  
284 associated temperatures – choice of calibration equations, continental inputs, lateral  
285 transport of the alkenones and isoGDGTs, ecology and seasonality of the source  
286 organisms of these lipids – will be considered in detail below.

287

288 5.2. Potential factors influencing the  $\text{U}_{37}^{\text{K}'}$  and  $\text{TEX}_{86}^{\text{H}}$  temperature estimates

289 5.2.1. Choice of the calibrations

290 The choice of the calibration has an influence on the absolute temperature estimates.

291 We tested the Temp- $\text{U}_{37}^{\text{K}'}$  annual calibration for the global ocean from 60 °N to 60 °S  
292 (Müller et al., 1998), the Temp- $\text{U}_{37}^{\text{K}'}$  SE Atlantic annual mean core top calibration (Müller  
293 et al., 1998) and the new Bayesian B-spline regression model, BAYSPLINE, for the  $\text{U}_{37}^{\text{K}'}$   
294 paleothermometer (Tierney and Tingley, 2018). The three calibrations resulted in highly  
295 similar temperatures (cf. Supp. Fig. 1). The annual calibration for the global ocean from  
296 60 °N to 60 °S resulted in Temp- $\text{U}_{37}^{\text{K}'}$  on average 0.8 °C warmer than the values obtained  
297 with the SE Atlantic annual calibration equation proposed by Müller et al. (1998). The  
298 Temp- $\text{U}_{37}^{\text{K}'}$  calibration by Tierney and Tingley (2018) resulted in Temp- $\text{U}_{37}^{\text{K}'}$  on average  
299 0.04 °C warmer than the values calculated with the SE Atlantic annual calibration  
300 equation proposed by Müller et al. (1998).

301 Using 53 core-top sediments, Ceccopieri et al. (2018) tested on a regional scale in the  
302 SSWA (SE Brazilian continental margin) the applicability of Temp- $\text{U}_{37}^{\text{K}'}$  calibrations by  
303 Müller et al. (1998) for the SE Atlantic: annual mean core top calibration (for  
304 temperatures from 0 to 27 °C) and seasonal (austral) calibrations. These authors  
305 concluded that the Temp- $\text{U}_{37}^{\text{K}'}$  SE Atlantic annual calibration (Müller et al., 1998) is  
306 comparable to SSWA annual mean present-day temperatures. Due to the high similarity  
307 between the Temp- $\text{U}_{37}^{\text{K}'}$  SE Atlantic annual mean core top calibration (Müller et al., 1998)

308 and Temp- $U_{37}^{K'}$  calibration by Tierney and Tingley (2018), both calibrations could be used  
309 interchangeably. In this work we adopt the most recent one.

310 Regarding GDGTs, we tested the Temp- $TEX_{86}^H$  calibration proposed by Kim et al.  
311 (2010), the Temp- $TEX_{86}^H(0-200)$  calibration by Kim et al. (2012), and the Temp- $TEX_{86}^H$   
312 and Temp- $TEX_{86}^H(0-200)$  calibrations by Tierney and Tingley (2014). The  $TEX_{86}^H$  and  
313  $TEX_{86}^H(0-200)$  calibrations by Tierney and Tingley (2014) resulted in a less pronounced  
314 temperature oscillation over time, and the absolute surface and subsurface values were  
315 closer to each other (cf. Supp. Fig. 2). The  $TEX_{86}^H$  calibration by Tierney and Tingley  
316 (2014) resulted in colder absolute temperatures than the  $TEX_{86}^H$  calibration by Kim et al.  
317 (2010). The  $TEX_{86}^H(0-200)$  calibration by Tierney and Tingley (2014) resulted in warmer  
318 absolute temperatures than the  $TEX_{86}^H(0-200)$  calibration by Kim et al. (2012).

319 The applicability of the Temp- $TEX_{86}^H$  calibration for regions with present-day  
320 temperatures from 15 to 30 °C proposed by Kim et al. (2010) was also tested by  
321 Ceccopieri et al. (2018) in the SSWA using the same core-top sediments as for the  $U_{37}^{K'}$   
322 investigation. Temp- $TEX_{86}^H$  was found to reflect the annual temperature in the SSWA.  
323 Although the Temp- $TEX_{86}^H$  by Tierney and Tingley (2014) are closer to the present-day  
324 temperature in GL-1090, we adopted Kim et al. (2010) calibration because its regional  
325 application in our study area was already validated by previous study.

326

### 327 5.2.2. Continental inputs

328 Temp- $TEX_{86}^H$  may be biased by isoprenoid GDGTs derived from terrigenous inputs  
329 and transported to the marine system by rivers and/or runoff (Schouten et al., 2013 and  
330 references therein). These inputs can notably be quantified by applying the BIT index  
331 (Hopmans et al., 2004), whose values close to 0 were generally associated with organic

332 material from open sea origin and those close to 1 (maximum value) with organic matter  
333 from terrestrial origin. In marine settings, BIT values above 0.4 were suggested to cause  
334 a deviation of the TEX<sub>86</sub> temperature estimates greater than 2.0 °C (Weijers et al., 2006).  
335 Nevertheless, care should be taken when interpreting the BIT values, as the two types of  
336 GDGTs used to calculate the BIT index - branched glycerol dialkyl glycerol tetraethers  
337 (brGDGTs) (Peterse et al., 2009; Sinninghe Damsté et al., 2009; Tierney et al., 2010) and  
338 crenarchaeol (Leininger et al., 2006; Weijers et al., 2006; Walsh et al., 2008) - can be  
339 produced in both terrestrial and aquatic environments. Therefore, in aquatic settings, high  
340 BIT values, which reflect a higher relative abundance of brGDGTs than that of  
341 crenarchaeol, could be associated with high terrestrial inputs of brGDGTs and/or *in situ*  
342 production of brGDGTs.

343 Along the core GL-1090, the BIT index varied between 0.11 and 0.92, with an average  
344 of  $0.45 \pm 0.12$  and higher values recorded during cold periods, from late MIS 6 to the  
345 onset of MIS 5e and during the onset of MIS 4 (cf. Supp. Fig. 3). Considering that  
346 previous studies have shown that no large river flows directly to the sea in this region  
347 (Conti and Furtado, 2006; Pessenda et al., 2012), terrestrial inputs were not expected to  
348 be high in the study area. To better evaluate this hypothesis, the behavior of organic and  
349 inorganic compounds from the same core was investigated, even though the latter are  
350 transported from the continent to marine sediments by different particles. No similar  
351 trends were observed between the BIT values and the Fe/Ca ratio - an inorganic proxy  
352 from continental runoff along the GL-1090 core (Figueiredo et al., 2020). The Fe/Ca  
353 peaks were not even registered by the BIT index or by Temp-TEX<sub>86</sub><sup>H</sup> (cf. Supp. Fig. 3).

354 However, the calcium ratios are influenced by sea level in the study area, embedding  
355 a very dominant low-frequency variability in the data. This sea level influence may  
356 suggest that the null correlation between BIT and XRF may not be substantially strong

357 evidence. Recently, Mathias et al. (2021) performed a deep sedimentological analysis on  
358 GL-1090 and they found very little river entry into the continental margin of southeastern  
359 Brazil during the Late Pleistocene. Although there was some continental influence, the  
360 results indicated the lowest terrigenous entries during MIS 5e and MIS 1. This suggests  
361 that the BIT values cannot be interpreted as recording high terrestrial inputs, since its  
362 highest values were found during MIS 5e. The high BIT values would rather be due to *in*  
363 *situ* production of brGDGTs at the GL-1090 sampling site, as observed in coastal regions  
364 (Crampton-Flood et al., 2019).

365

### 366 5.2.3. Lateral transport

367 The effect of lateral transport on  $U_{37}^{K'}$  temperature estimates has been reported in  
368 specific oceanic regions. Anomalously cold (by 2 °C – 6 °C)  $U_{37}^{K'}$  temperature values were  
369 found in sediments located under the Brazil–Malvinas Confluence and Malvinas Current  
370 in the southwestern Atlantic (Benthien and Muller, 2000). In this area of peculiar  
371 circulation, alkenone-bearing sediments are advected northwards carrying  $U_{37}^{K'}$  signals of  
372 their origin in cold waters. In the Campos Basin, SSWA, cold bias in  $U_{37}^{K'}$  derived  
373 temperatures were reported in core-top sediments close to the Cabo Frio Upwelling System  
374 and they were ascribed to alkenones advected from adjacent colder (upwelled) waters.

375 Considering that alkenones are more susceptible to lateral transport than isoGDGTs  
376 (Mollenhauer et al., 2007; Shah et al., 2008), Ceccopieri et al. (2018) suggested that  
377  $TEX_{86}^H$ -derived estimates better reflect local temperatures in this region in comparison  
378 with alkenones. In line with the conclusion of Ceccopieri et al. (2018), the lower absolute  
379 values of  $U_{37}^{K'}$  compared with those of  $TEX_{86}^H$  could be explained by intrusions of SACW  
380 into the photic zone identified in the GL-1090 during MIS 5e, 5c, and 5a substages due  
381 to the southward expansion of the Cabo Frio Upwelling System (Lessa et al. 2017).

382 Nevertheless, it should be noted that, while Lessa et al (2017) showed a vertical cooling  
383 only during warm substages, here Temp- $U_{37}^{K'}$  presented lower values than Temp-  
384  $TEX_{86}^H$  during the entire studied period (150 – 65 ka), indicating that the advection of cold  
385 water alone cannot explain the differences in  $TEX_{86}^H$  and  $U_{37}^{K'}$ -based temperature  
386 estimates. Additionally, the similar pattern and the high correlation between temperatures  
387 derived from the  $U_{37}^{K'}$  and  $TEX_{86}^H$  indices ( $r = 0.73$ ,  $p < 0.05$ ) suggest that either (i) the  
388 signals from the alkenones and isoGDGTs were produced vertically in the same area,  
389 probably at different depths in the water column, or (ii) the intensity of the lateral  
390 transport might differ over the investigated period, affecting both types of lipids in the  
391 same way during some periods. In any case, it means that lateral transport alone cannot  
392 explain the differences in absolute temperatures between  $U_{37}^{K'}$  and  $TEX_{86}^H$ .

393

#### 394 5.2.4. Seasonality

395 In a number of studies disparities between paleotemperatures reconstructed with the  
396  $U_{37}^{K'}$  and  $TEX_{86}^H$  indexes have been attributed to seasonal patterns in the production of the  
397 organisms, hapophyte algae and marine Thaumarchaeota, respectively (eg Lopes dos  
398 Santos et al., 2013; Auderset et al., 2019) but a consistent, globally applicable, seasonal  
399 pattern has not emerged.

400 Furthermore, compilation of sediment trap time series data have shown that the  
401 maximum alkenone flux across the oceans displays seasonal variations depending on  
402 local/regional oceanographic conditions and sedimentation processes (Mele and Prah  
403 2013). However, apart from few locations close to major hydrographic fronts,  
404 sedimentation patterns for  $U_{37}^{K'}$  in sediment trap time series appears provide a measure of  
405 annual mean SST.

406 The age of the GL-1090 core-top sample is 6.6 ka (Santos et al., 2017a), hampering  
407 its use to compare the seasonality of alkenone and isoGDGT source organisms -  
408 hapophyte algae and marine *Thaumarchaeota*, respectively - in the present-day.  
409 However, core-top studies in the SSWA shelf and slope (Cordeiro et al., 2014; Ceccopieri  
410 et al., 2018) have found that  $U_{37}^{K'}$ -derived temperature estimates agreed well with  
411 interpolated mean annual SST of ca. 24 °C. They also reported that, despite a likely most  
412 efficient export of isoGDGT during austral summer, core-top Temp- $TEX_{86}^H$  values were  
413 better correlated with the annual mean SST (Ceccopieri et al., 2018). In the regional  
414 context, Mahiques et al. (2005) analyzed alkenones in box cores near GL-1090 and  
415 considered Temp- $U_{37}^{K'}$  as reflecting mean annual temperatures over the last 700 years. A  
416 similar conclusion was drawn by Dauner et al. (2019), who showed that the temperature  
417 estimates derived from  $TEX_{86}^H$  and  $U_{37}^{K'}$  over the last 75 ka reflected the mean annual  
418 temperature in the SSWA.

419 Based on the afore-mentioned studies we argue that seasonal bias in the Temp- $TEX_{86}^H$   
420 and Temp- $U_{37}^{K'}$  estimates is of minor importance and that both  $TEX_{86}^H$  and  $U_{37}^{K'}$  indexes  
421 record the mean annual temperature in the study area.

422

#### 423 5.2.5. Water depth

424 Standard deviations of  $\pm 1.0$  °C for Temp- $U_{37}^{K'}$  (Müller et al., 1998) and  $\pm 2.5$  °C for  
425 Temp- $TEX_{86}^H$  (Kim et al., 2010) suggest that temperature differences of up to  $\pm 3.5$  °C  
426 between these proxies may be within the calibration error. The reconstructed mean  
427 temperature gradient ( $\Delta T$ ) of  $TEX_{86}^H$  and  $U_{37}^{K'}$  is 4.5 °C (Fig. 3b) and, therefore, higher  
428 than the calibration error. One explanation may be the difference of depth production  
429 between haptophytes and *Thaumarchaeota*.

430 Previous studies at the Campos Basin slope indicate that haptophyte algae, alkenone  
431 producers, inhabit the photic zone between 6 – 50 m depth (predominantly the 20 °C  
432 isotherm; Mahiques et al., 2009; Sousa et al., 2014; Rodrigues et al., 2014). This  
433 temperature isotherm corresponds to the interface between TW and SACW at the Santos  
434 Basin slope. Dauner et al. (2019) concluded that the temperatures derived from  $U_{37}^{K'}$  were  
435 consistent with those at around 30 m depth in the SSWA. Similarly, Luz (2019)  
436 considered that the  $U_{37}^{K'}$  signal reflected the temperature of the water column up to 25 m  
437 in the same region. This is consistent with previous studies in other areas, such as the  
438 Mediterranean Sea, the northern Arabian Sea, and in the tropical and subtropical Atlantic  
439 Ocean, which reported the possibility of alkenones recording temperature conditions  
440 below the surface (Ternois et al., 1997; Andruleit et al., 2003; Poulton et al., 2017).

441 IsoGDGT-producing archaea are generally more widely distributed in the water column  
442 than haptophytes, presenting a greater abundance between 40 and 150 m water depth  
443 (Lopes dos Santos et al., 2013; Kim et al., 2012; Schouten et al., 2002; Wuchter et al.,  
444 2006). In their study of the structure of the picoplankton community in a southern Atlantic  
445 transect, Zubkov et al. (2000) indicated that heterotrophic prokaryotes (bacteria and  
446 archaea) mainly inhabit the surface layer. While Dauner et al. (2019) confirmed that the  
447  $TEX_{86}^H$  signal represents the average annual temperature of the surface layer at the Santos  
448 Basin, Luz (2019) considered that Temp- $TEX_{86}^H$  reflects those of the water depths around  
449 100 - 200m, showing that there is no consensus on the depth of *Thaumarchaeota* growth  
450 in the SSWA.

451 Assuming that the non-thermal factors investigated in the previous sections (5.2.1,  
452 5.2.2, 5.2.3 and 5.2.4) do not cause significant deviations in temperature reconstructions,  
453 the results for the GL-1090 core suggest that the alkenones reflect temperatures at the

454 interface between the TW and the SACW, corresponding to the upper thermocline, and  
 455 the isoGDGTs reflect temperatures at the mixed layer of the Santos Basin slope.

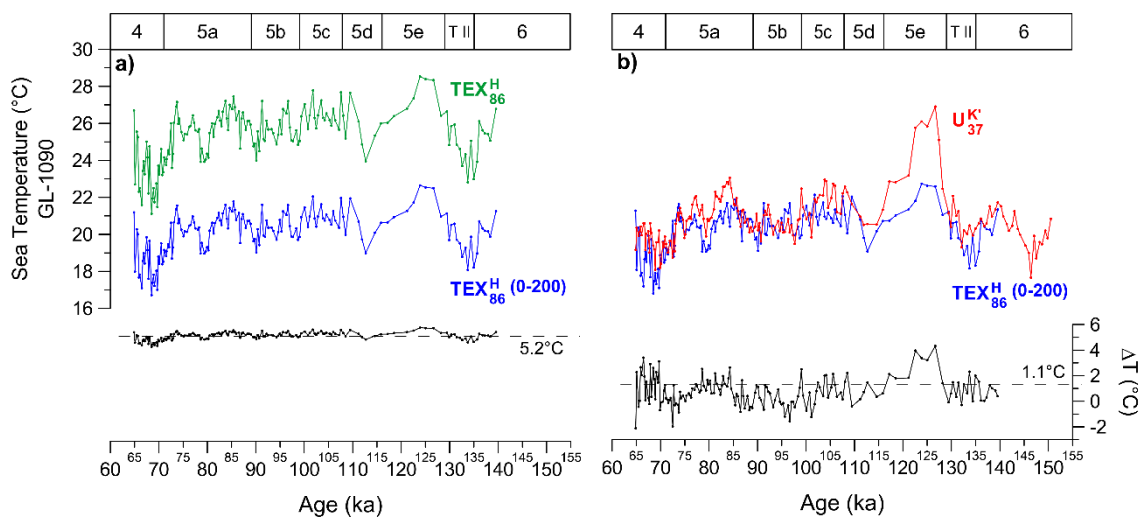
456

457 5.3. Multiproxy temperature reconstruction in the water column

458 In order to estimate the temperature gradient ( $\Delta T$ ) between the mixed layer and the  
 459 upper thermocline from GL-1090, Temp-TEX<sub>86</sub><sup>H</sup>(0-200) – for subsurface temperature –  
 460 was calculated and compared with Temp-TEX<sub>86</sub><sup>H</sup> – for surface temperature. The average  
 461  $\Delta T$  between Temp-TEX<sub>86</sub><sup>H</sup> and Temp-TEX<sub>86</sub><sup>H</sup>(0-200) was 5.2 °C (Fig. 4a), while the  
 462 average  $\Delta T$  between Temp-TEX<sub>86</sub><sup>H</sup>(0-200) and Temp-U<sub>37</sub><sup>K'</sup> was considerably smaller (less  
 463 than 1.0 °C) (Fig. 4b).

464 Ceccopieri et al. (2018) also applied the Temp-TEX<sub>86</sub><sup>H</sup>(0-200) calibration by Kim et al.  
 465 (2012) to core-top samples. At station A11 (Fig. 1b,c), these authors obtained values close  
 466 to instrumental data from WOA13 (Locarnini et al., 2013) depth-integrated temperatures  
 467 at about 100 - 200 m depth throughout the Campos Basin slope (between 13.8 °C and  
 468 21.7 °C). This suggests that the U<sub>37</sub><sup>K'</sup> signal at the GL-1090 site reflects the upper  
 469 thermocline temperature in the SSWA.

470

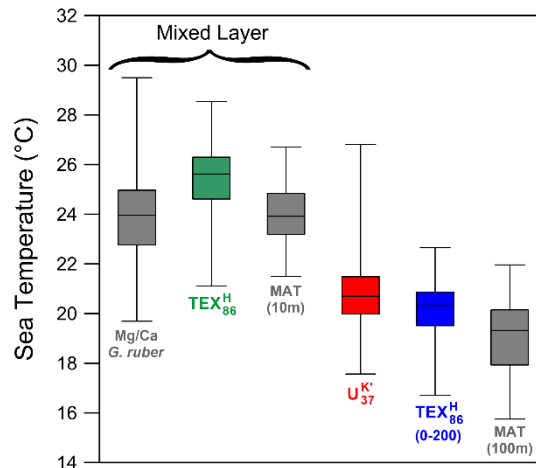


471

472 Fig. 4: Comparison of depth-integrated  $\text{TEX}_{86}^{\text{H}}(0-200)$  with  $\text{TEX}_{86}^{\text{H}}$  and  $\text{U}_{37}^{\text{K}'}$ -based  
473 temperatures, and their respective temperature gradients: a)  $\text{TEX}_{86}^{\text{H}}$  (green),  $\text{TEX}_{86}^{\text{H}}(0-$   
474  $200)$  (blue) and  $\Delta T$  ( $\text{TEX}_{86}^{\text{H}} - \text{TEX}_{86}^{\text{H}}(0-200)$ ) (black); b)  $\text{U}_{37}^{\text{K}'}$  (red),  $\text{TEX}_{86}^{\text{H}}(0-200)$  (blue)  
475 and  $\Delta T$  ( $\text{U}_{37}^{\text{K}'} - \text{TEX}_{86}^{\text{H}}(0-200)$ ) (black). Dashed lines mark the mean difference between the  
476 absolute temperatures derived from the organic proxies. Marine isotope stages (MIS) are  
477 highlighted on the upper x-axis. (For interpretation of the references to color in this figure  
478 legend, the reader is referred to the web version of this article.)

479  
480 The sea temperature estimates derived from  $\text{U}_{37}^{\text{K}'}$  and  $\text{TEX}_{86}^{\text{H}}$  were compared with those  
481 inferred for the same core from Mg/Ca *G. ruber* (Santos et al., 2017a) and from Modern  
482 Analog Technique (MAT) - a transfer function based on planktonic foraminiferal census  
483 count (Lessa et al., 2017) - at 10m (MAT-10m) and at 100m (MAT-100m) water depth.  
484 The Mg/Ca values published in Santos et al. (2017a) were converted to temperatures  
485 using the recent species-specific equation by Gray and Evans (2019). The calcification  
486 depth of *G. ruber* in the SSWA corresponds to the mixed layer (30 – 40m water depth),  
487 as shown by sediment traps studies (Venancio et al., 2017). This supports the use of the  
488 Mg/Ca proxy for reconstructing mixed layer temperatures in the region (eg Chiessi et al.,  
489 2007; Chiessi et al. 2014). Temp- $\text{TEX}_{86}^{\text{H}}$  values fall into the range of those derived from  
490 Mg/Ca and are close to MAT-10m temperatures, suggesting that these proxies reflect  
491 mixed layer temperatures (Fig. 5a).

492



493

494 Fig. 5: Comparison of paleotemperature ranges reconstructed from multiproxies at GL-  
 495 1090, between 150 and 65 ka: temperature (°C) derived from Mg/Ca *G. ruber* (gray) (after  
 496 Santos et al., 2017a); TEX<sub>86</sub><sup>H</sup> (green) (this study); MAT-10m (gray) (Lessa et al., 2017);  
 497 U<sub>37</sub><sup>K'</sup> (red) (this study); TEX<sub>86</sub><sup>H</sup>(0-200) (blue) (this study); and MAT-100m (gray) (Lessa et  
 498 al., 2017). (For interpretation of the references to color in this figure legend, the reader is  
 499 referred to the web version of this article.)

500

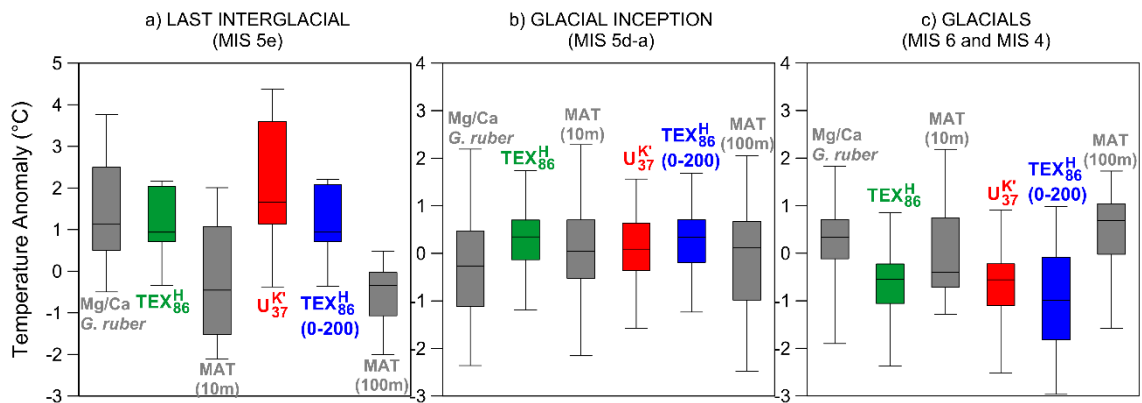
501 In contrast, the range of temperatures derived from U<sub>37</sub><sup>K'</sup> is similar to the ones from  
 502 TEX<sub>86</sub><sup>H</sup>(0-200) and MAT-100 m. The corresponding estimates are lower than Mg/Ca,  
 503 TEX<sub>86</sub><sup>H</sup> and MAT-10m-based temperatures, suggesting that, in core GL-1090, Temp-U<sub>37</sub><sup>K'</sup>  
 504 recorded temperatures from the upper thermocline. This is consistent with the fact that,  
 505 in the SSWA, haptophytes reach their maximum abundance where the deep chlorophyll  
 506 maximum occurs, above the thermocline (Brandini et al., 2014; Rodrigues et al., 2014;  
 507 Ribeiro et al., 2016). Dauner et al. (2019) also attributed to the depth of the haptophyte  
 508 habitat the lower Temp-U<sub>37</sub><sup>K'</sup> than Temp-TEX<sub>86</sub><sup>H</sup> over the last 75 ka in the SSWA, and this  
 509 condition seems to be the most likely to explain why the temperatures derived from U<sub>37</sub><sup>K'</sup>  
 510 are more similar to the temperatures from the upper thermocline than from the mixed  
 511 layer in GL-1090, between 150 and 65 ka (Fig. 5b).

512

513 5.4. Regional dynamics in the water column in the SSWA during MIS 5e

514 During the MIS 5e (129-116 ka) and the onset of MIS 4 (71-65 ka), the  $\Delta T$  between  
515  $TEX_{86}^H$  and  $U_{37}^{K'}$  was lower than the average one over the whole core GL-1090 (Fig. 3b).  
516 During the MIS 5e, the  $\Delta T$  was reduced due to a more prominent warming of  $U_{37}^{K'}$ . In  
517 contrast, during the onset of the MIS 4, this decrease could be explained by a more  
518 pronounced cooling of  $TEX_{86}^H$ . If we assume that the source organisms of alkenones and  
519 isoGDGTs live at different depths, then a change in the thermal structure of the photic  
520 zone may explain the similar temperatures between the mixed layers and the upper  
521 thermocline during MIS 5e and the onset of MIS 4. The pronounced positive temperature  
522 anomaly derived from  $U_{37}^{K'}$  during MIS 5e (Fig. 6a) suggests greater heat storage at the  
523 upper thermocline.

524



525

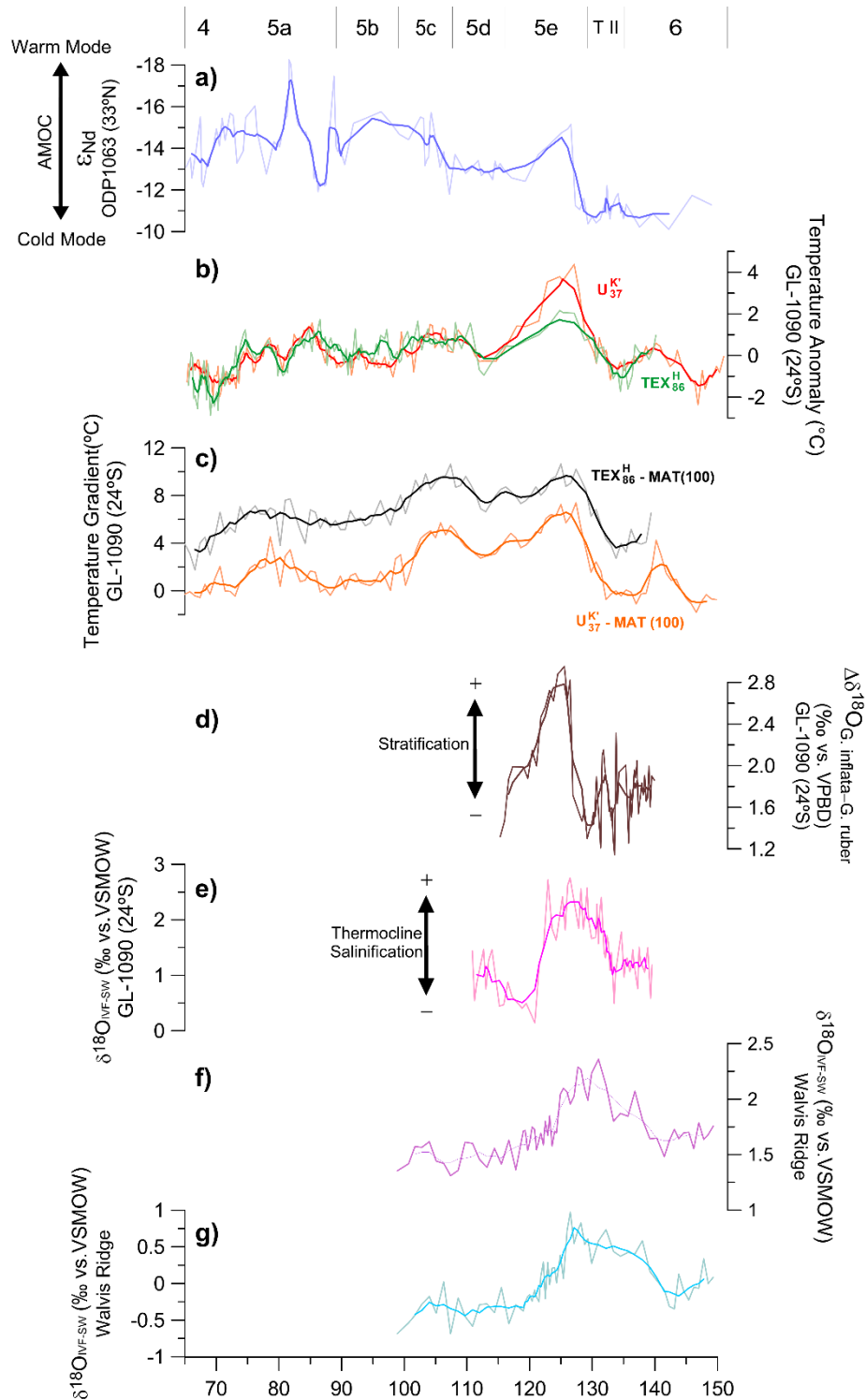
526 Fig. 6: Temperature anomalies normalized by the standard deviation of each proxy along  
527 the core GL-1090 for three time intervals: (a) Last Interglacial (LIG/MIS 5e); (b) Glacial  
528 inception (MIS 5d-a); (c) Glacials (MIS 6 and MIS 4), based on Mg/Ca *G. ruber* (gray)  
529 (after Santos et al., 2017a);  $TEX_{86}^H$  (green) (this study); MAT-10m (gray) (Lessa et al.,  
530 2017);  $U_{37}^{K'}$  (red) (this study);  $TEX_{86}^H$ (0-200) (blue) (this study); and MAT-100m (gray)

531 (Lessa et al., 2017). (For interpretation of the references to color in this figure legend, the  
532 reader is referred to the web version of this article.)

533

534 During the LIG period (Figure 6a),  $U_{37}^{K'}$  recorded a steep thermal gradient in the upper  
535 thermocline, which decreased in the middle/end of the interglacial complex scenario  
536 (Figure 6b). The intensity of this thermal gradient was further reduced in the glacial  
537 scenario (Figure 6c). The evaluation of these different water column temperature profiles  
538 over time suggests that alkenones are more strongly affected by changes in depth  
539 conditions than isoGDGTs, the latter being directly affected by the vertical mixing  
540 temperature oscillation. This explains why  $U_{37}^{K'}$ -based temperatures are similar to those of  
541 the surface layer during the LIG and close to the subsurface temperatures during the  
542 glacials.

543



544

545 Figure 7: Comparison of temperature anomalies from core GL-1090 with other low/mid-  
 546 paleoclimate signals from 150 to 65 ka: a)  $\epsilon_{Nd}$  record of core ODP1063 (Böhm et al.,  
 547 2015); b) Temperature anomalies from core GL-1090 based on  $TEX_{86}^H$  (green) and  $U_{37}^{K'}$   
 548 (red) (this study); c) Temperature gradient from core GL-1090 based on  $TEX_{86}^H$  (this study)  
 549 minus MAT-100m (Lessa et al., 2017; green), and  $U_{37}^{K'}$  (this study) minus MAT-100m (Lessa et  
 550 al., 2017; red); d)  $\Delta\delta^{18}O$  (*Globorotalia inflata* – *Globigerinoides ruber*) (Santos et al.,

551 2017); e) Thermocline  $\delta^{18}\text{O}_{\text{IVC-SW}}$  values from core GL-1090 (Ballalai et al., 2019)  
552 estimated from Mg/Ca ratio-derived thermocline temperatures; f) Surface  $\delta^{18}\text{O}_{\text{IVC-SW}}$   
553 values from core 64PE- 174P13 (Walvis Ridge) (Scussolini et al., 2015) estimated from  
554 *Globigerinoides ruber*  $\delta^{18}\text{O}$  values; g) Thermocline  $\delta^{18}\text{O}_{\text{IVC-SW}}$  values from core 64PE-  
555 174P13 (Walvis Ridge) (Scussolini et al., 2015) estimated from *Globigerinoides*  
556 *truncatulinooides*  $\delta^{18}\text{O}$  values. Marine isotope stages (MIS) are highlighted on the upper  
557 x-axis. (For interpretation of the references to color in this figure legend, the reader is referred to  
558 the web version of this article.)  
559

560 Furthermore, during MIS 5e and MIS 5c, the high  $\Delta T$  between the organic proxies  
561  $\text{U}_{37}^{\text{K}^1}/\text{TEX}_{86}^{\text{H}}$  and MAT-100 (Fig. 7) suggests upper ocean stratification with the flattening  
562 of the mixed layer, which may have reduced the downward diffusion of heat. This  
563 decrease in vertical mixing due to enhanced stratification is shown by  $\Delta\delta^{18}\text{O}$  (*G. inflata*  
564 - *G. ruber*) (Fig. 7d). Leonhardt et al. (2013) analyzed fossil assemblages of  
565 coccolithophorids, *Globigerinoides ruber* and corresponding stable oxygen isotopes from  
566 a sediment core collected in the SSWA, covering the last 130 ka. The authors observed  
567 lower surface productivity during MIS 5e, which was related to an increase in the  
568 nutricline depth, making surface water fertilization impossible.

569 During late MIS 6 / T II and the onset of MIS 4, sea temperature positive anomalies  
570 (Fig. 7b) were associated with the weakening of the AMOC and consequent strengthening  
571 of the BC due to changes in circulation structure (Broecker, 1998; Santos et al., 2017).  
572 The  $\epsilon\text{Nd}$ , a water mass provenance proxy used for interpretation of water mass geometry  
573 from the Bermuda Rise (Böhm et al., 2015), corroborates this hypothesis (Fig. 7a).

574 It is known that warm and saline Subtropical Indian Ocean water is transported into  
575 the South Atlantic through the Indian-Atlantic oceanic gateway (Gordon, 1986;  
576 Lutjeharms, 2006; Beal et al., 2011). Marino et al. (2013) point that the salinity increase  
577 between 138 ka and 130 ka indicated by  $\delta^{18}\text{O}_{\text{SW}}$  represents an interhemispheric coupling

578 once it is correlated with abrupt swings in the North Atlantic. According to Marino et al.  
579 (2013), the Indian-to-Atlantic salt transport is a strong driver of the AMOC during the  
580 abrupt climate changes of the Late Pleistocene.

581 Ballalai et al. (2019) analyzed thermocline Mg/Ca-derived temperatures and salinity  
582 from ice volume-corrected  $\delta^{18}\text{O}$  seawater ( $\delta^{18}\text{O}_{\text{IVC-SW}}$ ) records in GL-1090 during  
583 Termination II and early Late Interglacial (Fig. 7e). According to these authors, during  
584 the intensification of the Agulhas Leakage, starting from ca. 142 ka BP (Fig. 7f; g), the  
585 salt anomaly was recirculated within the South Atlantic subtropical gyre instead of being  
586 immediately transmitted to the North Atlantic due to a “barrier” caused by an ocean-  
587 atmosphere coupling that increased the BC flow and limited its equatorial crossing. Our  
588 findings are consistent with those of Ballalai et al. (2019). In this sense, this study confirm  
589 the connection between the intensification of the Agulhas Leakage and the heat storage  
590 at the upper thermocline in the SSWA during MIS 5e.

591 In summary, our organic data from GL-1090 provided information on the applicability  
592 of the  $U_{37}^K$  and  $\text{TEX}_{86}^H$  proxies in the SSWA and have enabled the identification of a  
593 change in the thermocline structure in the SSWA from late MIS 6 to the onset of MIS 4.  
594 Based on our results, we suggest that alkenones were more affected by warm temperatures  
595 at the upper thermocline during the LIG period (MIS 5e), and isoGDGTs were more  
596 affected by cold temperatures at the mixed layer during glacial (MIS 6 and MIS 4).  
597 However, more studies covering the same time range with atmospheric modeling and  
598 thermocline proxies in the South Atlantic must be considered in future research studies  
599 in the region in order to better understand the mechanisms that led to these scenarios.

600

601 6. CONCLUSIONS

602 This work presents the first temperature reconstruction based on alkenones and  
603 isoGDGTs covering late MIS 6 to the onset of MIS 4 in the SSWA. A multiproxy  
604 approach was developed, involving the organic proxies  $U_{37}^{K'}$  and  $TEX_{86}^H$ , as well as  
605 previously published data (Mg/Ca ratio and MAT derived from planktonic foraminifera).  
606 Non-thermal factors, i.e. terrestrial inputs and lateral transport, were suggested to have  
607 minor influence on the temperature signal derived from alkenones/isoGDGTs.  $TEX_{86}^H$   
608 and  $U_{37}^{K'}$  temperature estimates were assumed to reflect different water depths, i.e. those  
609 of the mixed layer and the upper thermocline, respectively. This was related to the  
610 different habitat depths of the source organisms of isoGDGTs and alkenones - marine  
611 *Thaumarchaeota* and hapophyte algae, respectively.

612 Our downcore record emphasizes the relevance of a multiproxy approach to bringing  
613 insights into the interpretation of the response of each proxy in the same sediment core,  
614 leading to better understanding of the paleoceanographic changes from 150 ka to 65 ka,  
615 mainly during the LIG, in the south-eastern Brazilian margin. Our results suggest that a  
616 steep thermal gradient in the upper thermocline exists during the LIG, as does a reduced  
617 thermal gradient in the glacial scenario. Finally, our study demonstrates that the organic  
618 proxies applied here are reliable for reconstructing paleoceanographic changes in the  
619 SSWA.

620

#### 621 CRediT AUTHORSHIP CONTRIBUTION STATEMENT

622 Joana F. Cruz: writing – original draft, formal analysis, conceptualization. Alice M. S.  
623 Rodrigues, Thiago P. Santos, Igor M. Venancio, Douglas Lessa, Rodrigo L. Sobrinho,  
624 Rodrigo A. Nascimento: writing – review & editing. Ioanna Bouloubassi, Arnaud Huguet:  
625 formal analysis, review & editing. Marcelo C. Bernardes: supervision, formal analysis,  
626 review & editing.

627

628 DECLARATION OF COMPETING INTEREST

629 The authors declare that they have no known competing financial interests or personal  
630 relationships that could have appeared to influence the work reported in this paper.

631

632 ACKNOWLEDGEMENTS

633 We thank Petrobras for providing the sediment core used in this research, and Vincent  
634 Klein (LOCEAN-Sorbonne Université) and Christelle Anquetil (METIS-Sorbonne  
635 Université) for their support during the analyses. This study was supported by  
636 CAPES/Paleocean Project (23038.001417/2014-7), CAPES-IODP/Aspecto Project  
637 (88887.091731/2014-01), Project CLIMATE/Print-CAPES (88887.310301/2018-00)  
638 and Finance Code 001, INSU-CNRS program LEFE (BARISTA project) and partially by  
639 CNPq Project 429767/2018-8. Joana F. Cruz thank for her CNPq (140443/2016-9) and  
640 CAPES/Programas Estratégicos (88881.145911/2017-01) support. This study was  
641 financed in part by CNPq Project RAIN (grant 406322/2018-0). This study was also  
642 funded by FAPERJ (SEI-260003/000677/2023), which currently financially supports  
643 Igor M. Venancio with a JCNE grant (200.120/2023 – 281226).

644

645 REFERENCES

646 Andruleit, H., Stager, S., Rogalla, U., Cepek, P., 2003. Living coccolithophores in the  
647 northern Arabian Sea: ecological tolerances and environmental control, *Mar.*  
648 *Micropaleontol.*, 49, 157-181, [https://doi.org/10.1016/S0377-8398\(03\)00049-5](https://doi.org/10.1016/S0377-8398(03)00049-5).

649 Auderset, A., Martínez-García, A., Tiedemann, R., Hasenfratz, A.P., Eglinton, T.I.,  
650 Schiebel, R., Sigman, D.M., Haug, G.H., 2019. Gulf Stream intensification after the early

651 Pliocene shoaling of the Central American Seaway, *Earth Planet. Sci. Lett.*, 520, 268–  
652 278, <https://doi.org/10.1016/j.epsl.2019.05.022>.

653 Ausín, B., Magill, C., Haghypour, N., Fernández, Á., Wacker, L., Hodell, D., Baumann,  
654 K.-H., Eglinton, T.I., 2019. (In)coherent multiproxy signals in marine sediments:  
655 Implications for high-resolution paleoclimate reconstruction, *Earth Planet. Sci. Lett.*, 515,  
656 38–46, <https://doi.org/10.1016/j.epsl.2019.03.003>.

657 Ballalai, J.M., Santos, T.P., Lessa, D.O., Venancio, I.M., Chiessi, C.M., Johnstone,  
658 H.J.H., Kuhnert, H., Claudio, M.R., Toledo, F., Costa, K.B., Albuquerque, A.L.S. 2019.  
659 Tracking spread of the Agulhas leakage into the western South atlantic and its northward  
660 transmission during the last interglacial. *Paleoceanog. and Paleoclimatol.*, [s. l.], v. 34, n.  
661 11, p. 1744-1760, doi: 10.1029/2019PA003653.

662 Bazin, L., Landais, A., Lemieux-Dudon, B., Toyé Mahamadou Kele, H., Veres, D.,  
663 Parrenin, F., Martinerie, P., Ritz, C., Capron, E., Lipenkov, V.Y., Loutre, M.-F.; Raynaud,  
664 D., Vinther, B.M., Svensson, A.M., Rasmussen, S.O., Severi, M., Blunier, T.,  
665 Leuenberger, M.C., Fischer, H., Masson-Delmotte, V., Chappellaz, J.A., Wolff, E.W.  
666 2013. An optimized multi-proxy, multi-site Antarctic ice and gas orbital chronology  
667 (AICC2012): 120-800 ka. *Climate of the Past*, [s. l.], v. 9, n. 4, 1715-1731,  
668 <https://doi.org/10.5194/cp-9-1715-2013>.

669 Beal, L.M., De Ruijter, W.P.M., Biastoch, A., Zahn, R., 2011. On the role of the Agulhas  
670 system in ocean circulation and climate, *Nature*, 472 (7344), 429–436.,  
671 <https://doi.org/10.1038/nature09983>.

672 Benthien, A., Müller, P.J., 2000. Anomalously low alkenone temperatures caused by  
673 lateral particle and sediment transport in the Malvinas Current region, western Argentine

674 Basin, *Deep-Sea Res. Part I Oceanogr. Res. Pap.*, 47, 2369–2393,  
675 [https://doi.org/10.1016/S0967-0637\(00\)00030-3](https://doi.org/10.1016/S0967-0637(00)00030-3).

676 Blaauw, M., Christeny, J.A., 2011. Flexible paleoclimate age-depth models using an  
677 autoregressive gamma process, *Bayesian Anal.*, 6, 457–474, doi:10.1214/11-BA618.

678 Böhm, E.; Lippold, J.; Gutjahr, M.; et al, 2015. Strong and deep Atlantic meridional  
679 overturning circulation during the last glacial cycle. *Nature*, v. 517, n. 7534, p. 73–76.

680 Brandini, F.P., Nogueira Jr, M., Simião, M., Codina, J.C.U., Noernberg, M.A., 2014.  
681 Deep chlorophyll maximum and plankton community response to oceanic bottom  
682 intrusions on the continental shelf in the South Brazilian Bight, *Cont. Shelf Res.*, 89, 61–  
683 75, <https://doi.org/10.1016/j.csr.2013.08.002>.

684 Brassell, S.C., Eglinton, G., Marlowe, I.T., Pflaumann, U., Sarnthein, M., 1986.  
685 Molecular stratigraphy: a new tool for climatic assessment, *Nature*, 320, 129–133,  
686 <https://doi.org/10.1038/320129a0>.

687 Campos, E.J.D., Miller, J.L., Moiler, T.J., Peterson, R.G., 1995. Physical oceanography  
688 of the Southwest Atlantic Ocean, *Oceanography*, 8, 87-91,  
689 <https://doi.org/10.5670/oceanog.1995.03>.

690 Campos, E.J.D., Velhote, D., Silveira, I.C.A., 2000. Shelf break upwelling driven by  
691 Brazil current cyclonic meanders, *Geophys. Res. Lett.*, 27, 751-754,  
692 <https://doi.org/10.1029/1999GL010502>.

693 Capron, E., Govin, A., Stone, E.J., Masson-Delmotte, V., Mulitza, S., Otto-Bliesner,  
694 B., Rasmussen, T.L., Sime, L.C., Waelbroeck, C., Wolff, E.W., 2014. Temporal and  
695 spatial structure of multi-millennial temperature changes at high latitudes during the Last

696 Interglacial, *Quat. Sci. Rev.*, 103, 116-133, [https://doi.org/10.1016/j.quascirev.2014.08.](https://doi.org/10.1016/j.quascirev.2014.08.018)  
697 018.

698 Ceccopieri, M., Carreira, R.S., Wagener, A.L.R., Hefter, J., Mollenhauer, G., 2018. On  
699 the application of alkenone- and GDGT-based temperature proxies in the southeastern  
700 Brazilian continental margin, *Org. Geochem.*, 126, 43-56,  
701 <https://doi.org/10.1016/j.orggeochem.2018.10.009>.

702 Chiessi, C.M., Ulrich, S., Mulitza, S., Pätzold, J., Wefer, G., 2007. Signature of the Brazil-  
703 Malvinas Confluence (Argentine Basin) in the isotopic composition of planktonic  
704 foraminifera from surface sediments. *Mar. Micropaleontol.*, 64, 1–2, 52–66,  
705 <https://doi.org/10.1016/j.marmicro.2007.02.002>.

706 Chiessi, C.M., Mulitza, S., Groeneveld, J., Silva, J.B., Campos, M.C., Gurgel, M.H.C.,  
707 2014. Variability of the Brazil Current during the late Holocene. *Palaeogeogr.*  
708 *Palaeoclimatol. Palaeoecol.*, 415, 28–36, <http://dx.doi.org/10.1016/j.palaeo.2013.12.005>.

709 Chiessi, C.M., Mulitza, S., Mollenhauer, G., Silva, J.B., Groeneveld, J., Prange, M., 2015.  
710 Thermal evolution of the western South Atlantic and the adjacent continent during  
711 Termination 1, *Clim. Past*, 11, 915–929, <https://doi.org/10.5194/cp-11-915-2015>.

712 Conti, L.A., Furtado, V.V., 2006. Geomorfologia da Plataforma Continental do Estado  
713 de São Paulo, *Braz. J. Geol.*, 36 (2): 305-312.

714 Costa, K.B.; Cabarcos, E.; Santarosa, A.C.A.; Battaglin, B.B.F.; Toledo, F.A.L., 2016. A  
715 multiproxy approach to the climate and marine productivity variations along MIS 5 in SE  
716 Brazil: A comparison between major components of calcareous nannofossil assemblages  
717 and geochemical records. *Palaeogeography, Palaeoclimatology, Palaeoecology*,  
718 Amsterdam, v. 449, p. 275–288.

719 Cordeiro, L.G.M.S., Belem, A.L., Bouloubassi, I., Rangel, B., Sifeddine, A., Capilla, R.,  
720 Albuquerque, A.L.S., 2014. Reconstruction of southwestern Atlantic sea surface  
721 temperatures during the last Century: Cabo Frio continental shelf (Brazil), *Palaeogeogr.*  
722 *Palaeoclimatol. Palaeoecol.*, 415, 225–232, <https://doi.org/10.1016/j.palaeo.2014.01.020>.

723 Crampton-Flood, E.D., Peterse, F., Sinninghe Damsté, J.S., 2019. Production of branched  
724 tetraethers in the marine realm: Svalbard fjord sediments revisited, *Org. Geochem.*, 138,  
725 103907, <https://doi.org/10.1016/j.orggeochem.2019.103907>.

726 Dauner, A.L.L., Mollenhauer, G., Bicego, M.C., de Souza, M.M., Nagai, R.H., Figueira,  
727 R.C.L., Mahiques, M.M., de Melo e Souza, S.H., Martins, C.C., 2019. Multi-proxy  
728 reconstruction of sea surface and subsurface temperatures in the western South Atlantic  
729 over the last ~75 kyr. *Quat. Sci. Rev.*, 215, 22–34.  
730 <https://doi.org/10.1016/j.quascirev.2019.04.020>.

731 Evangelista, H., Gurgel, M., Sifeddine, A., Rigozo, N.R., Boussafir, M., 2014. South  
732 Tropical Atlantic anti-phase response to Holocene Bond Events, *Palaeogeogr.*  
733 *Palaeoclimatol. Palaeoecol.*, 415, 21–27, <https://doi.org/10.1016/j.palaeo.2014.07.019>.

734 Figueiredo, T.S., Santos, T.P., Costa, K.B., Toledo, F., Albuquerque, A.L.S., Smoak,  
735 J.M., Bergquist, B.A., Silva-Filho, E.V., 2020. Effect of deep Southwestern Subtropical  
736 Atlantic Ocean circulation on the biogeochemistry of mercury during the last two  
737 glacial/interglacial cycles, *Quat. Sci. Rev.*, 239, 106368,  
738 <https://doi.org/10.1016/j.quascirev.2020.106368>.

739 Gordon, A.L., 1986. Inter-ocean exchange of thermocline water, *J. Geophys. Res.*,  
740 91(C4), 5037–5046.

741 Govin, A., Chiessi, C.M. , Zabel, M., Sawakuchi, A.O., Heslop, D., Hörner, T., Zhang,  
742 Y., Mulitza, S., 2014. Terrigenous input off northern South America driven by changes  
743 in Amazonian climate and the North Brazil Current retroflexion during the last 250 ka,  
744 *Clim. Past*, 10, 2, 843–862, <http://dx.doi.org/10.5194/cp-10-843-2014>.

745 Govin, A., Capron, E., Tzedakis, P.C., Verheyden, S., Ghaleb, B., Hillaire-Marcel, C., St-  
746 Onge, G., Stoner, J.S., Bassinot, F., Bazin, L., Blunier, T., Combourieu-Nebout, N., El  
747 Ouahabi, A., Genty, D., Gersonde, R., Jimenez-Amat, P., Landais, A., Martrat, B.,  
748 Masson-Delmotte, V., Parrenin, F., Seidenkrantz, M.S., Veres, D., Waelbroeck, C., Zahn,  
749 R., 2015. Sequence of events from the onset to the demise of the Last Interglacial:  
750 Evaluating strengths and limitations of chronologies used in climatic archives, *Quat. Sci.*  
751 *Rev.*, 129, 1–36, <http://doi.org/10.1016/j.quascirev.2015.09.018>.

752 Gray, W.R., Evans, D. 2019. Nonthermal influences on Mg/Ca in planktonic  
753 foraminifera: a review of culture studies and application to the last glacial maximum.  
754 *Paleoceanography and Paleoclimatology*, [s. l.], v. 34, p. 306-315,  
755 <https://doi.org/10.1029/2018PA003517>.

756 Hansen, J., Sato, M., Hearty, P., Ruedy, R., Kelley, M., Masson-Delmotte, V., Russell,  
757 G., Tselioudis, G., Cao, J., Rignot, E., Velicogna, I., Tormey, B., Donovan, B., Kandiano,  
758 E., von Schuckmann, K., Kharecha, P., Legrande, A.N., Bauer, M., Lo, K.-W., 2016. Ice  
759 melt, sea level rise and superstorms: evidence from paleoclimate data, climate modeling,  
760 and modern observations that 2.0 °C global warming could be dangerous, *Atmos. Chem.*  
761 *Phys.*, 16, 3761–3812, <https://doi.org/10.5194/acp-16-3761-2016>.

762 Hoffman, J.S., Clark, P.U., Parnell, A.C., He, F. 2017. Regional and global sea-surface  
763 temperatures during the last interglaciation. *Science*, [s. l.], v. 355, p. 276- 279.

764 Hopmans, E.C., Weijers, J.W.H., Schefuß, E., Herfort, L., Sinninghe Damsté, J.S.,  
765 Schouten, S., 2004. A novel proxy for terrestrial organic matter in sediments based on  
766 branched and isoprenoid tetraether lipids, *Earth Planet. Sci. Lett.*, 224, 107–116,  
767 <https://doi.org/10.1016/j.epsl.2004.05.012>.

768 Huguet, A., Fosse, C., Laggoun-Défarge, F., Delarue, F., Derenne, S., 2013. Effects of a  
769 short-term experimental microclimate warming on the abundance and distribution of  
770 branched GDGTs in a French peatland, *Geochim. Cosmochim. Acta.*, 105, 294-315,  
771 <https://doi.org/10.1016/j.gca.2012.11.037>.

772 Huguet, A., Coffinet, S., Roussel, A., Gayraud F., Anquetil, C., Bergonzini, L.,  
773 Bonanomi, G., Williamson, D., Majule A., Derenne, S., 2019. Evaluation of 3-hydroxy  
774 fatty acids as a pH and temperature proxy in soils from temperate and tropical altitudinal  
775 gradients, *Org. Geochem.*, 129, 1-13, <https://doi.org/10.1016/j.orggeochem.2019.01.002>.

776 Huguet, C., Martrat, B., Grimalt, J.O., Sinninghe Damsté, J.S., Schouten, S., 2011.  
777 Coherent millennial-scale patterns in  $U_{37}^{K'}$  and  $TEX_{86}^H$  temperature records during the  
778 penultimate interglacial-to-glacial cycle in the western Mediterranean,  
779 *Paleoceanography*, 26, PA2218, <https://doi.org/10.1029/2010PA002048>.

780 Kim, J.H., van der Meer, J., Schouten, S., Helmke, P., Willmott, V., Sangiorgi, F., Koç,  
781 N., Hopmans, E.C., Sinninghe Damsté, J.S., 2010. New indices and calibrations derived  
782 from the distribution of crenarchaeal isoprenoid tetraether lipids: implications for past sea  
783 surface temperature reconstructions, *Geochim. Cosmochim. Acta*, 74, 4639-4654,  
784 <https://doi.org/10.1016/j.gca.2010.05.027>.

785 Kim, J., Romero, O.E., Lohmann, G., Donner, B., Laepple, T., Haam, E., Sinninghe  
786 Damsté, J.S., 2012. Pronounced subsurface cooling of North Atlantic waters off

787 Northwest Africa during Dansgaard-Oeschger interstadials. *Earth Planet. Sci. Lett.*, 340,  
788 95–102, doi: 10.1016/j.epsl.2012.05.018.

789 Leduc, G., Schneide, R., Kim, J.-H., Lohmann, G., 2010. Holocene and Eemian sea  
790 surface temperature trends as revealed by alkenone and Mg/Ca paleothermometry, *Quat.*  
791 *Sci. Rev.*, 29, 989–1004, <https://doi.org/10.1016/j.quascirev.2010.01.004>.

792 Leininger, S., T. Urich, M. Schloter, L. Schwark, J. Qi, G. Nicol, J. Prosser, S. Schuster,  
793 and C. Schleper, 2006. Archaea predominate among ammonia- oxidizing prokaryotes in  
794 soils, *Nature*, 442, 806–809, doi:10.1038/nature04983.

795 Leonhardt, A., Toledo, F.A.L., Coimbra, J.C., 2013. The productivity history in the  
796 southwestern atlantic as inferred from coccolithophore record for the last 130 kyr, *Rev.*  
797 *bras. paleontol.* 16(3):361-374.

798 Lessa, D.V.O., Ramos, R.P., Barbosa, C.F., da Silva, A.R., Belem, A., Turcq, B.,  
799 Albuquerque, A.L.S., 2014. Planktonic foraminifera in the sediment of a western  
800 boundary upwelling system off Cabo Frio, Brazil, *Mar. Micropaleontol.*, 106, 55–68,  
801 <https://doi.org/10.1016/j.marmicro.2013.12.003>.

802 Lessa, D.V.O., Venancio, I.M., dos Santos, T.P., Belem, A.L., Turcq, B.J., Sifeddine, A.,  
803 Albuquerque, A.L.S., 2016. Holocene oscillations of Southwest Atlantic shelf circulation  
804 based on planktonic foraminifera from an upwelling system (off Cabo Frio, Southeastern  
805 Brazil), *The Holocene*, 26, 1175–1187, <https://doi.org/10.1177/0959683616638433>.

806 Lessa, D.V.O., Santos, T.P., Venancio, I.M., Albuquerque, A.L.S., 2017. Offshore  
807 expansion of the Brazilian coastal upwelling zones during Marine Isotope Stage 5, *Glob.*  
808 *Planet. Change*, 158, 13–20, <https://doi.org/10.1016/j.gloplacha.2017.09.006>.

809 Lisiecki, L.E., Raymo, M.E., 2005. A Pliocene-Pleistocene stack of 57 globally  
810 distributed benthic  $\delta^{18}\text{O}$  records, *Paleoceanography*, 20, 1, 1–17,  
811 <https://doi.org/10.1029/2004PA001071>.

812 Locarnini, R.A., Mishonov, A.V., Antonov, J.I., Boyer, T.P., Garcia, H.E., Baranova,  
813 O.K., Zweng, M.M., Paver, C.R., Reagan, J.R., Johnson, D.R., Hamilton, M., Seidov, D.,  
814 2013. *World Ocean Atlas 2013, Volume 1: Temperature*. NOAA Atlas NESDIS.

815 Lopes dos Santos, R.A., Spooner, M.I., Barrows, T.T., De Deckker, P., Sinninghe  
816 Damsté, J.S., Schouten, S., 2013. Comparison of organic ( $\text{U}_{37}^{\text{K}}$ ,  $\text{TEX}_{86}^{\text{H}}$ , LDI) and faunal  
817 proxies (foraminiferal assemblages) for reconstruction of late Quaternary sea surface  
818 temperature variability from offshore southeastern Australia, *Paleoceanography*, 28, 377–  
819 387, <https://doi.org/10.1002/palo.20035>.

820 Lourenço, R.A., Mahiques, M.M., Wainer, I.E.K.C., Rosell-Melé, A., Bicego, M.C.,  
821 2016. Organic biomarker records spanning the last 34,800 years from the southeastern  
822 Brazilian upper slope: links between sea surface temperature, displacement of the Brazil  
823 Current, and marine productivity, *Geo Mar. Lett.*, 36, 361-369,  
824 <https://doi.org/10.1007/s00367-016-0453-7>.

825 Lutjeharms, J.R.E., 2006. *The Agulhas Current*, 329 pp., Springer, Berlin.

826 Luz, L.G., Santos, T.P., Eglinton, T.I., Montluçon, D., Ausin, B., Haghypour, N., Sousa,  
827 S.M., Nagai, R.H., Carreira, R.S., 2020. Contrasting late-glacial paleoceanographic  
828 evolution between the upper and lower continental slope of the western South Atlantic.  
829 *Climate of the Past*, [s. l.], v. 16, p. 1245-1261.

830 Luz, L.G., 2019. Mudanças oceanográficas e climáticas nos últimos 50 mil anos no  
831 sudoeste do Atlântico com base em registros de paleo-indicadores orgânicos e

832 inorgânicos na Margem Continental do Rio de Janeiro, Brasil. 188 f. Thesis (PhD in  
833 Chemistry) - Pontifícia Universidade Católica do Rio de Janeiro, Rio de Janeiro, Brazil.

834 Mahiques, M.M., Silveira, I.C.A., Sousa, S.H.M., Fukumoto, M.M., 2005. Modern  
835 sedimentation in the Cabo Frio upwelling system, *An. Acad. Bras. Ciênc.*, 77, 535–548,  
836 <http://dx.doi.org/10.1590/S0001-37652005000300013>.

837 Mahiques, M.M., Coaracy Wainer, I.K., Burone, L., Nagai, R., Sousa, S.H.M., Figueira,  
838 R.C.L., Silveira, I.C.A., Bicego, M.C., Pavani, V.A.D., Hammer, Ø. 2009. A high-  
839 resolution Holocene record on the Southern Brazilian shelf: Paleoenvironmental  
840 implications. *Quaternary International*, [s. l.], v. 206, n. 1–2, p. 52-61.

841 Mann, M., Bradley, R., Hughes, M., 1998. Global-Scale Temperature Patterns and  
842 Climate Forcing Over the Past Six Centuries, *Nature*, 392, 779-787,  
843 <https://doi.org/10.1038/33859>.

844 Marino, G., Zahn, R., Ziegler, M., Purcell, C., Knorr, G., Hall, I. R., Ziveri, P., Elderfield,  
845 H., 2013. Agulhas salt-leakage oscillations during abrupt climate changes of the Late  
846 Pleistocene, *Paleoceanography*, 28, 599–606, doi:10.1002/palo.20038.

847 Mathias, G. L., Roud, S. C., Chiessi, C. M., Campos, M. C., Dias, B. B., Santos, T. P., et  
848 al., 2021. A multiproxy approach to unravel late Pleistocene sediment flux and bottom  
849 water conditions in the western South Atlantic Ocean. *Paleoceanography and  
850 Paleoclimatology*, 36, e2020PA004058. <https://doi.org/10.1029/2020PA004058>.

851 Mollenhauer, G., Inthorn, M., Vogt, T., Zabel, M., Sinninghe Damsté, J.S., Eglinton, T.I.,  
852 2007. Aging of marine organic matter during cross-shelf lateral transport in the Benguela  
853 upwelling system revealed by compound-specific radiocarbon dating. *Geochemistry,  
854 Geophysics, Geosystems* 8, Q09004, doi:10.1029/2007GC001603.

855 Müller, P.J., Kirst, G., Ruhland, G., von Storch, I., Rosell-Melé, A., 1998. Calibration of  
856 the alkenone paleotemperature index  $U_{37}^{K'}$  based on core-tops from the eastern South  
857 Atlantic and the global ocean (60 °N – 60 °S), *Geochim. Cosmochim. Acta*, 62, 1757–  
858 1772, [https://doi.org/10.1016/S0016-7037\(98\)00097-0](https://doi.org/10.1016/S0016-7037(98)00097-0).

859 Otto-Bliesner, B.L., Rosenbloom, N., Stone, E.J., Mckay, N.P., Lunt, D.J., Brady, E.C.,  
860 Overpeck, J.T. 2013. How warm was the last interglacial? New model–data comparisons.  
861 *Philosophical Transactions of the Royal Society A, London*, v. 371, 20130097, doi:  
862 10.1098/rsta.2013.0097.

863 Otto-Bliesner, B., Braconnot, P., Harrison, S.P., Lunt, D.J., Abe-Ouchi, A., Albani, S.,  
864 Bartlein, P., Capron, E., Carlson, A., Dutton, A., Fischer, H., Goelzer, H., Govin, A.,  
865 Haywood, A., Joos, F., LeGrande, A., Lipscomb, W., Lohmann, G., Mahowald, N.,  
866 Nehrbass-Ahles, C., Peterschmitt, J.Y., Pausata, F.S.-R., Phipps, S., Renssen, H., 2016.  
867 Two Interglacials: Scientific Objectives and Experimental Designs for CMIP6 and  
868 PMIP4 Holocene and Last Interglacial Simulations, *Clim. Past Discussions*, 1-36,  
869 <https://doi.org/10.5194/cp-2016-106>.

870 Past Interglacials Working Group of PAGES, 2016. Interglacials of the last 800,000  
871 years, *Rev. Geophys.*, 54, 162–219, doi:10.1002/2015RG000482.

872 Pereira, L.S., Arz, H.W., Pätzold, J., Portilho-Ramos, R.C., 2018. Productivity evolution  
873 in the South Brazilian Bight during the last 40,000 years. *Paleoceanogr. Paleocl.*, 33,  
874 <https://doi.org/10.1029/2018PA003406>.

875 Pessenda, L.C.R., Vidotto, E., De Oliveira, P.E., Buso, A.A., Cohen, M.C.L., Rossetti,  
876 D.F., Ricardi-Branco, F.B., Bendassolli, J.A., 2012. Late Quaternary vegetation and  
877 coastal environmental changes at Ilha do Cardoso mangrove, southeastern Brazil,

878 Palaeogeogr. Palaeoclimatol. Palaeoecol., 363-364, 57-68,  
879 <https://doi.org/10.1016/j.palaeo.2012.08.014>.

880 Peterse, F., Kim, J.- H., Schouten, S., Kristensen, D.K., Koç, N., Sinninghe Damsté, J.  
881 S., 2009. Constraints on the application of the MBT/CBT palaeothermometer at high  
882 latitude environments (Svalbard, Norway), *Org. Geochem.*, 40, 692–699,  
883 [doi:10.1016/j.orggeochem.2009.03.004](https://doi.org/10.1016/j.orggeochem.2009.03.004).

884 Peterson, R.G., Stramma, L., 1991. Upper-level circulation in the South Atlantic Ocean,  
885 *Prog. Oceanogr.*, 26, 1–73, [https://doi.org/10.1016/0079-6611\(91\)90006-8](https://doi.org/10.1016/0079-6611(91)90006-8).

886 Piola, A.R., Matano, R.P., 2001. Brazil and Falklands (Malvinas) currents. In: Steele, J.  
887 H., Thorpe, S. A., Turekian, K. K. (Eds.), *Ocean Currents: A Derivative of the*  
888 *Encyclopedia of Ocean Sciences*, Elsevier Inc., 35-43, [https://doi.org/10.1016/B978-0-](https://doi.org/10.1016/B978-0-12-409548-9.10541-X)  
889 [12-409548-9.10541-X](https://doi.org/10.1016/B978-0-12-409548-9.10541-X).

890 Piola, A.R., Campos, E.J.D., Möller Jr., O.O., Charo, M., Martinez, C., 2000. Subtropical  
891 Shelf Front off eastern South America, *J. Geophys. Res. Ocean.*, 105, 6565-6578,  
892 <https://doi.org/10.1029/1999JC000300>.

893 Pivel, M.A.G., Santarosa, A.C.A., Toledo, F.A.L., Costa, K.B., 2013. The Holocene onset  
894 in the southwestern South Atlantic, *Palaeogeogr. Palaeoclimatol. Palaeoecol.*, 374, 164–  
895 172, <https://doi.org/10.1016/j.palaeo.2013.01.014>.

896 Portilho-Ramos, R.C., Ferreira, F., Calado, L., Frontalini, F., Toledo, M.B., 2015.  
897 Variability of the upwelling system in the southeastern Brazilian margin for the last  
898 110,000 years, *Glob. Planet. Chang.*, 135, 179–189,  
899 <https://doi.org/10.1016/j.gloplacha.2015.11.003>.

900 Poulton, A.J., Holligan, P.M., Charalampopoulou, A., Adey, T.R., 2017. Coccolithophore  
901 ecology in the tropical and subtropical Atlantic Ocean: New perspectives from the  
902 Atlantic meridional transect (AMT) programme, *Prog. Oceanogr.*, 158, 150–170,  
903 <https://doi.org/10.1016/j.pocean.2017.01.003>.

904 Prah, F.G., Wakeham, S.G., 1987. Calibration of unsaturation patterns in long-chain  
905 ketone compositions for palaeotemperature assessment, *Nature*, 330, 367–369,  
906 <https://doi.org/10.1038/330367a0>.

907 Ribeiro, C.G., Lopes dos Santos, A., Marie, D., Pellizari, V.H., Brandini, F.P., Vaultot,  
908 D., 2016. Pico and nanoplankton abundance and carbon stocks along the Brazilian Bight,  
909 *Peer, J* 4, e2587, <https://doi.org/10.7717/peerj.2587>.

910 Richardson, P.L., 2007. Agulhas leakage into the Atlantic estimated with subsurface  
911 floats and surface drifters, *Deep-Sea Res. Part I Oceanogr. Res. Pap.*, 54, 8, 1361–1389,  
912 <https://doi.org/10.1016/j.dsr.2007.04.010>.

913 Rodrigues, S.V., Marinho, M.M., Cubas Jonck, C.C., Gonçalves, E.S., Brant, V.F.,  
914 Paranhos, R., Curbelo, M.P., Falcão, A.P., 2014. Phytoplankton community structures in  
915 shelf and oceanic waters off southeast Brazil (20 ° - 25 °S), as determined by pigment  
916 signatures, *Deep. Res. Part I Oceanogr. Res. Pap.*, 88, 47-62,  
917 <http://dx.doi.org/10.1016/j.dsr.2014.03.006>.

918 Santos, T.P., Lessa, D.O., Venancio, I.M., Chiessi, C.M., Mulitza, S., Kuhnert, H., Govin,  
919 A., Machado, T., Costa, K.B., Toledo, F., Dias, B.B., Albuquerque, A.L.S., 2017a.  
920 Prolonged warming of the Brazil Current precedes deglaciations. *Earth Planet. Sci. Lett.*,  
921 463, 1–12, <http://dx.doi.org/10.1016/j.epsl.2017.01.014>.

922 Santos, T.P., Lessa, D.O., Venancio, I.M., Chiessi, C.M., Mulitza, S., Kuhnert, H.,  
923 Albuquerque, A.L.S., 2017b. The impact of the AMOC resumption in the western South  
924 Atlantic thermocline at the onset of the Last Interglacial. *Geophys. Res. Lett.*, 44, 11, 547-  
925 554, <https://doi.org/10.1002/2017GL074457>.

926 Santos, T.P., Ballalai, J.M., Franco, D.R., Oliveira, R.R., Lessa, D.O., Venancio, I.M.,  
927 Chiessi, C.M.; Kuhnert, H., Johnstone, H., Albuquerque, A.L.S., 2020. Asymmetric  
928 response of the subtropical western South Atlantic thermocline to the Dansgaard-  
929 Oeschger events of Marine Isotope Stages 5 and 3. *Quat. Sci. Rev.*, Oxford, v. 237, n.  
930 106307.

931 Schlitzer, R., 2013. Ocean Data View, <http://www.awi-bremerhaven.de/GEO/ODV>.

932 Schmid, C., 2014. Mean vertical and horizontal structure of the subtropical circulation in  
933 the South Atlantic from three-dimensional observed velocity fields, *Deep. Res. Part I*  
934 *Oceanogr. Res. Pap.*, 91, 50-71, <https://doi.org/10.1016/j.dsr.2014.04.015>.

935 Schouten, S., Hopmans, E.C., Schefuß, E., Sinninghe Damsté, J.S., 2002. Distributional  
936 variations in marine crenarchaeol membrane lipids: a new tool for reconstructing ancient  
937 sea water temperatures?, *Earth Planet. Sci. Lett.*, 204, 265–274, doi: 10.1016 / S0012-  
938 821X (02) 00979-2.

939 Schouten, S., Hopmans, E.C., Sinninghe Damsté, J.S., 2013. The organic geochemistry  
940 of glycerol dialkyl glycerol tetraether lipids: A review. *Org. Geochem.* 54, 19-61.

941 Scussolini, P., Marino, G., Brummer, G.- J. A., Peeters, F. J. C., 2015. Saline Indian  
942 Ocean waters invaded the South Atlantic thermocline during glacial termination II.  
943 *Geology*, 43(2), 139–142. <https://doi.org/10.1130/G36238.1>.

944 Shah, S.R., Mollenhauer, G., Ohkouchi, N., Eglinton, T.I., Pearson, A., 2008. Origins of  
945 archaeal tetraether lipids in sediments: Insights from radiocarbon analysis. *Geochimica*  
946 *et Cosmochimica Acta* 72, 4577–4594.

947 Silveira, I.C.A., Schmidt, A.C.K., Campos, E.J.D., Godoi, S.S., Ikeda, Y., 2000. A  
948 corrente do Brasil ao largo da costa leste brasileira, *Rev. Bras. Oceanogr.*, 48, 171-183,  
949 <https://doi.org/10.1590/S1413-77392000000200008>.

950 Sinninghe Damsté, J.S., Ossebaar, J., Abbas, B., Schouten, S., Verschuren, D., 2009.  
951 Fluxes and distribution of tetraether lipids in an equatorial African lake: Constraints on  
952 the application of the TEX86 palaeothermometer and BIT index in lacustrine settings,  
953 *Geochim. Cosmochim. Acta*, 73, 4232–4249, doi:10.1016/j.gca.2009.04.022.

954 Sousa, S.H.M., De Godoi, S.S., Amaral, P.G.C., Vicente, T.M., Martins, M.V.A., Sorano,  
955 M.R.G.S., Mahiques, M.M., 2014. Distribution of living planktonic foraminifera in  
956 relation to oceanic processes on the southeastern continental Brazilian margin (23 °S –  
957 25 °S and 40 °W – 44 °W). *Continental Shelf Research*, Oxford, v. 89, p. 76-87.

958 Stramma, L., England, M., 1999. On the water masses and mean circulation of the South  
959 Atlantic Ocean, *J. Geophys. Res. Ocean.*, 104, 20863–20883,  
960 <https://doi.org/10.1029/1999JC900139>.

961 Ternois, Y., Sicre, M.A., Boireau, A., Conte, M.H., Eglinton, G., 1997. Evaluation of  
962 long-chain alkenones as paleo-temperature indicators in the Mediterranean Sea. *Deep-*  
963 *Sea Res. Part I Oceanogr. Res. Pap.*, 44, 271–286, <https://doi.org/10.1029/96PA00041>.

964 Tierney, J.E., Russell, J.M., Eggermont, H., Hopmans, E.C., Verschuren, D., Sinninghe  
965 Damsté, J.S., 2010. Environmental controls on branched tetraether lipid distributions in

966 tropical East African lake sediments, *Geochim. Cosmochim. Acta*, 74, 4902–4918,  
967 doi:10.1016/j.gca.2010.06.002.

968 Tierney, J. E., Tingley, M., P., 2014. A Bayesian, spatially-varying calibration model for  
969 the TEX<sub>86</sub> proxy, *Geochim. Cosmochim. Acta*, 127, 83–186,  
970 <http://dx.doi.org/10.1016/j.gca.2013.11.026>.

971 Tierney, J. E., Tingley, M., P., 2018. BAYSPLINE: A new calibration for the alkenone  
972 paleothermometer, *Paleoceanography and Paleoclimatology*, 33, 281–301,  
973 <https://doi.org/10.1002/2017PA003201>.

974 Turney, C.S.M., Jones, R.T., 2010. Does the Agulhas Current amplify global  
975 temperatures during super-interglacials?, *J. Quat. Sci.*, 25, 6, 839–843,  
976 <https://doi.org/10.1002/jqs.1423>.

977 Venancio, I.M., Belem, A.L., Lessa D.O., Albuquerque, A.L.S., Mulitza, S., Schulz, M.,  
978 Kucera, M., 2017. Calcification depths of planktonic foraminifera from the southwestern  
979 Atlantic derived from oxygen isotope analyses of sediment trap material, *Mar.*  
980 *Micropaleontol.*, 136, 37–50, <https://doi.org/10.1016/j.marmicro.2017.08.006>.

981 Veres, D., Bazin, L., Landais, A., Toyé Mahamadou Kele, H., Lemieux- Dudon, B.,  
982 Parrenin, F., Martinerie, P., Blayo, E., Blunier, T., Capron, E., Chappellaz, J., Rasmussen,  
983 S. O., Severi, M., Svensson, A., Vinther, B., Wolff, E. W., 2013. The Antarctic ice core  
984 chronology (AICC2012): an optimized multi- parameter and multi-site dating approach  
985 for the last 120 thousand years. *Climate of the Past*, [s. l.], v. 9, p. 1733–1748,  
986 doi:10.5194/cp-9-1733-2013.

987 Wainer, I., Prado, L.F., Khodri, M., Otto-Bliesner, B., 2014. Reconstruction of the South  
988 Atlantic Subtropical Dipole index for the past 12,000 years from surface temperature  
989 proxy, *Sci. Rep.*, 4, 5291, <https://doi.org/10.1038/srep05291>.

990 Walsh, E.M., Ingalls, A.E., Keil, R.G., 2008. Sources and transport of terrestrial organic  
991 matter in Vancouver Island fjords and the Vancouver–Washington Margin: A multiproxy  
992 approach using  $\delta^{13}\text{C}_{\text{org}}$ , lignin phenols, and the ether lipid BIT index, *Limnol.*  
993 *Oceanogr.*, 53, 1054–1063, doi:10.4319/lo.2008.53.3.1054.

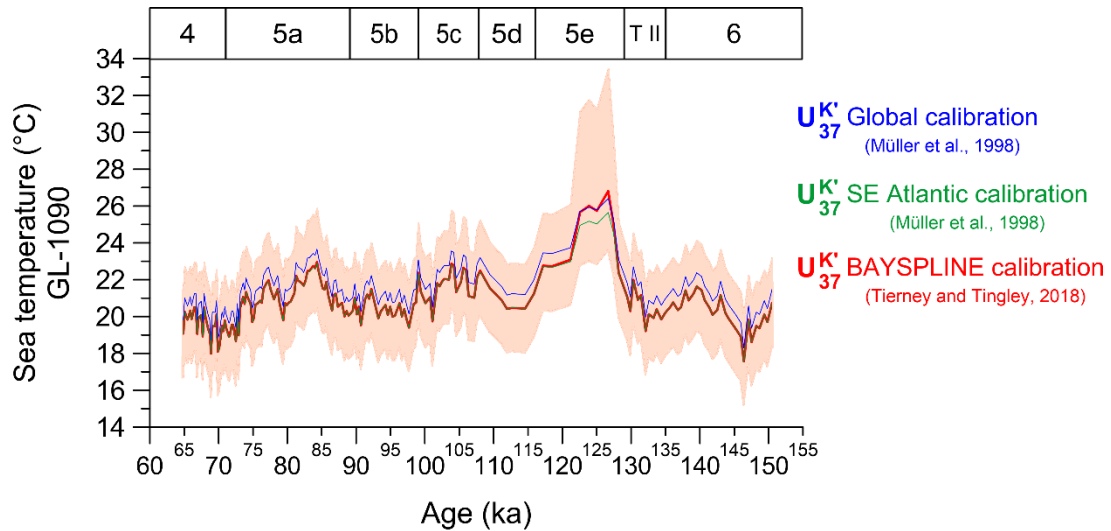
994 Weijers, J.W.H., Schouten, S., Spaargaren, O.C., Sinninghe Damsté, J.S., 2006.  
995 Occurrence and distribution of tetraether membrane lipids in soils: implications for the  
996 use of the TEX86 proxy and the BIT index, *Org. Geochem.*, 37, 1680–1693,  
997 <https://doi.org/10.1016/j.orggeochem.2006.07.018>.

998 Wuchter, C., Schouten, S., Coolen, M.J.L., Sinninghe Damsté, J.S., 2004. Temperature-  
999 dependent variation in the distribution of tetraether membrane lipids of marine  
1000 Crenarchaeota: Implications for TEX86 paleothermometry. *Paleoceanography*,  
1001 Washington, v. 19, p. 1–10.

1002 Zubkov, M.V., Sleigh, M.A., Burkill, P.H., Leakey, R.J.G., 2000. Picoplankton  
1003 community structure on the Atlantic Meridional Transect: a comparison between seasons.  
1004 *Progress in Oceanography*, Oxford, v. 45, p. 369-386.

1005

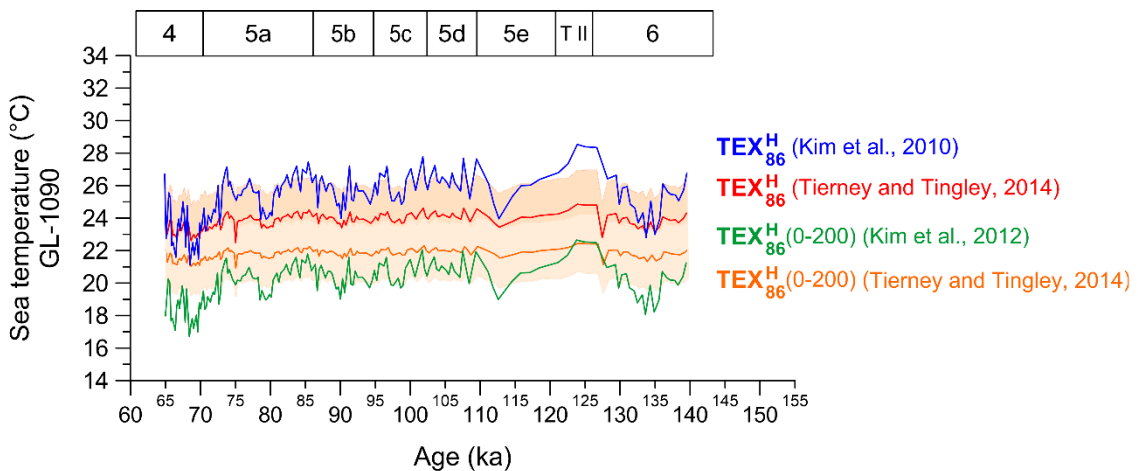
1006 SUPPLEMENTARY MATERIAL



1007

1008 Supp. Fig. 1: Temp- $U_{37}^{K'}$  Global calibration - annual average (Müller et al., 1998) (blue),  
 1009 Temp- $U_{37}^{K'}$  SE Atlantic calibration - annual average (Müller et al., 1998) (green), and  
 1010 Temp- $U_{37}^{K'}$  BAYSPLINE calibration (Tierney and Tingley, 2018) (red) - red shading  
 1011 represents the 95% confidence interval. Marine isotope stages (MIS) are highlighted on the  
 1012 upper x-axis. (For interpretation of the references to color in this figure legend, the reader  
 1013 is referred to the web version of this article.)

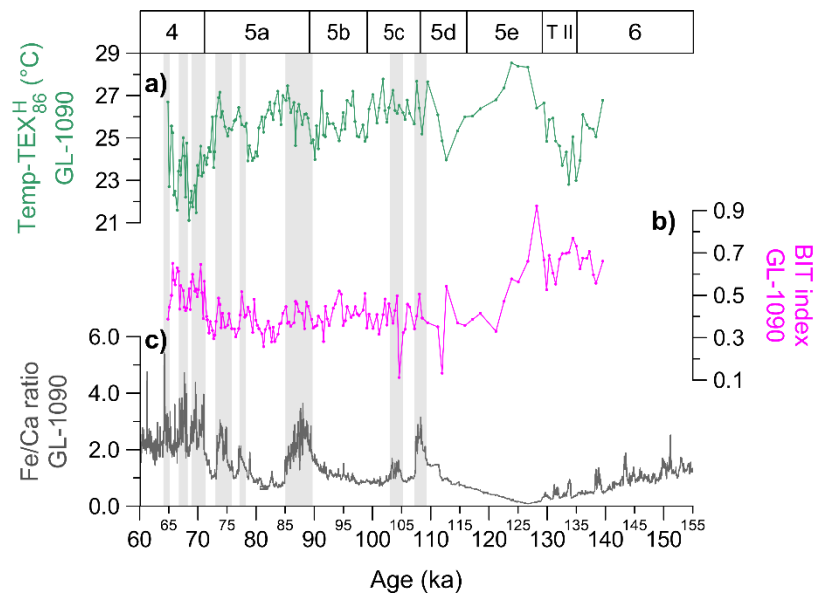
1014



1015

1016 Supp. Fig. 2: Temp- $TEX_{86}^H$  Global calibration - annual average ( $> 15$  °C) (Kim et al.,  
 1017 2010) (blue), Temp- $TEX_{86}^H$  (0-200) Global calibration - annual average (Kim et al., 2012)  
 1018 (green), Temp- $TEX_{86}^H$  Bayesian calibration (Tierney and Tingley, 2014) (red) - red shading

1019 represents the 95% confidence interval, and SubTemp-TEX<sub>86</sub><sup>H</sup> Bayesian calibration  
 1020 (Tierney and Tingle, 2014) (orange) - orange shading represents the 95% confidence  
 1021 interval. Marine isotope stages (MIS) are highlighted on the upper x-axis. (For  
 1022 interpretation of the references to color in this figure legend, the reader is referred to the  
 1023 web version of this article.)  
 1024



1025  
 1026 Supp. Fig. 3: Comparison between (a) Temp-TEX<sub>86</sub><sup>H</sup> (green) (this study), (b) BIT index  
 1027 (pink) (this study) and (c) Fe/Ca ratio (gray) (Figueiredo et. al, 2020). Gray bars indicate  
 1028 peaks in Fe/Ca ratios. Marine isotope stages (MIS) are highlighted on the upper x-axis.  
 1029 (For interpretation of the references to color in this figure legend, the reader is referred to  
 1030 the web version of this article.)